ESAIM: M2AN 60 (2026) 945–980
https://doi.org/10.1051/m2an/2026023

ESAIM: Mathematical Modelling and Numerical Analysis
www.esaim-m2an.org

A NON-CONVEX VARIATIONAL MODEL FOR JOINT POLYENERGETIC CT RECONSTRUCTION, SENSOR DENOISING AND MATERIAL DECOMPOSITION

Georgios Papanikos[1,*] and Benedikt Wirth[2]

Abstract. Computed Tomography (CT) is widely used in engineering and medicine for imaging the interior of objects, patients, or animals. If the employed X-ray source is monoenergetic, image reconstruction essentially means the inversion of a ray transform. Typical X-ray sources are however polyenergetic (*i.e.* emit multiple wavelengths, each with different attenuation behaviour), and ignoring this fact may lead to artefacts such as beam hardening. An additional difficulty in some settings represents the occurrence of two different types of noise, the photon counting effect on the detector and the electronic noise generated *e.g.* by CCD cameras. We propose a novel variational image reconstruction model that takes both noise types and the polyenergetic source into account and moreover decomposes the reconstruction into different materials based on their different attenuation behaviour. In addition to a detailed mathematical analysis of the model we put forward a corresponding iterative algorithm including its convergence analysis. Numerical reconstructions of phantom data illustrate the feasibility of the approach.

Mathematics Subject Classification. 90C30, 49M37, 65K10, 65R32, 45Q05.

Received August 31, 2024. Accepted February 15, 2026.

1. Introduction

Transmission X-ray Computed Tomography (CT) is a non-invasive imaging technique applied in many research areas such as engineering and medicine since it allows the visualization of internal structures of objects, humans, and animals [2,30]. To this end X-rays are sent through the imaged object in different directions, and for each ray one records the remaining intensity behind the object. Typically one uses so-called polyenergetic or polychromatic X-ray sources that emit X-rays at different wavelengths. However, common CT scanners only record the accumulated (over all wavelengths) ray intensity behind the object (known as single energy CT, SECT), while scanners that separately measure the remaining intensity in two or even more different regions of the wavelength spectrum (dual energy CT, DECT, and spectral CT, respectively) are substantially more complicated and thus expensive and rare.

Keywords and phrases. Polyenergetic computed tomography, variational image reconstruction model, material decomposition, photon counting noise, electronic noise.

[1] Department of Mathematics, University of Manchester, Manchester, UK.
[2] Department of Mathematics, University of Münster, Münster, Germany.
*Corresponding author: papaniksgeo@gmail.com

We propose a variational model to reconstruct the spatial distribution of a number of known materials from SECT measurements with a polychromatic X-ray source, accounting at the same time for photon counting Poisson noise at the different wavelengths as well as additional electronic Gaussian noise. It is given by the minimization of the functional

$$F(y, \boldsymbol{w}) = \frac{1}{2\sigma^2}\int_\Sigma \left(f - \int_{E_{\min}}^{E_{\max}} y \,\mathrm{d}\mathcal{L}^1 \right)^2 \mathrm{d}\mathcal{H}^n + \int_\Sigma \int_{E_{\min}}^{E_{\max}} d_{\mathrm{KL}}(y, \mathcal{I}(\boldsymbol{w})) \,\mathrm{d}\mathcal{L}^1 \,\mathrm{d}\mathcal{H}^n + R^{\alpha,\beta}(\boldsymbol{w}) \tag{1.1}$$

over the material density function $\boldsymbol{w}$ and the wavelength-dependent sinograms y (see Sect. 2.2). In more detail, $\boldsymbol{w}(\boldsymbol{x}) \in \mathbb{R}^{N_{\mathrm{mat}}}$ indicates the fractions of the N_{mat} different materials at position $\boldsymbol{x}$, while $y(E, \boldsymbol{x}, \boldsymbol{\theta})$ describes the number of photons of wavelength (or photon energy) E arriving at a position $(\boldsymbol{x}, \boldsymbol{\theta})$ in the sinogram domain. The measurement $f(\boldsymbol{x}, \boldsymbol{\theta})$, in contrast, does not distinguish different wavelengths. Furthermore, $\sigma \in \mathbb{R}$ denotes the standard deviation of the electronic Gaussian noise, d_{KL} denotes the so-called Kullback–Leibler divergence, $\mathcal{I}(\boldsymbol{w})$ denotes the forward operator (turning the material distribution $\boldsymbol{w}$ into the expected photon intensity at every wavelength and sinogram position). The first two integrals act as data discrepancy terms: The first penalizes the deviation (due to electronic detector noise) of the measurement from the reconstructed photon count accumulated over all photon energies of the X-ray source. The second penalizes reconstructed photon counts y that are statistically unlikely (with respect to the underlying physical Poisson distribution) given a guess $\boldsymbol{w}$ of the material distribution. Here, forward operator $\mathcal{I}$ is based on the divergent beam transform (which describes the X-ray beam geometry of typical CT scanners) and models the attenuation of each ray depending on the photon energy. Finally, $R^{\alpha,\beta}(\boldsymbol{w})$ represents a regularization functional with regularization weights $\alpha, \beta > 0$,

$$R^{\alpha,\beta}(\boldsymbol{w}) = \alpha \sum_{i=1}^{N_{\mathrm{mat}}} \mathrm{TV}(w_i) + \int_\Omega \iota_\Delta(\boldsymbol{w}) \,\mathrm{d}\mathcal{L}^n + \frac{\beta}{2}\int_\Omega -|\boldsymbol{w} - \mathbf{1}/N_{\mathrm{mat}}|^2 \,\mathrm{d}\mathcal{L}^n.$$

The first term penalizes the so-called total variation $\mathrm{TV}(w_i)$ of the different material distributions, which for piecewise constant w_i (as desired) measures the perimeter of all constant regions weighted with the jump in w_i between neighbouring regions. It leads to smooth boundaries between different material regions and is required mathematically to prevent fractal boundaries (which could potentially better accommodate the measurement noise). The second term constrains the material fractions to the probability simplex Δ (ι_Δ denotes the corresponding convex indicator function) in order to allow solely physically possible material fractions. The integrand of the last term gets minimal for pure materials and thus presents an incentive to decompose the reconstruction domain $\Omega \subset \mathbb{R}^n$ $(n = 2, 3)$ into regions of pure materials.

This model merges different strands from the literature concerning beam hardening correction (BHC, in particular due to explicit photon energy modelling), material decomposition (MD, *via* reconstructing material fractions), and noise modelling (by separating the effects of electronic and quantum mechanical photon noise). These three aspects are actually closely related and interdependent so that their joint treatment in (1.1) is quite natural. Beside this model, our first main contribution is its rigorous mathematical well-posedness analysis (which also implies the well-posedness of previous variational models dealing with only one aspect). The second contribution is the design of a corresponding iterative scheme based on the works of Brune [5], Sawatzky [44] and Papanikos [37] (which concern image reconstruction from positron emission tomography (PET) measurements and monoenergetic transmission tomography measurements with Poisson and mixed Gaussian–Poisson noise, respectively), including its rigorous proof of convergence to a critical point of (1.1). The proposed algorithm alternatingly updates the variables y and $\boldsymbol{w}$, where for given $\boldsymbol{w}$ there exists an explicit formula for optimal y, while for given y the update in $\boldsymbol{w}$ splits into a data and a regularization step. The algorithm is efficient in the regime of medium to strong regularization, while for low regularization (in case of very low noise) it may require too many iterations, which is why we also provide two alternative primal-dual-based algorithms in the appendix. Though our work is more theoretical in nature we finally also illustrate the model feasibility in phantom reconstruction studies.

1.1. Conceptual motivation and benefits of our approach

Ignoring the polychromaticity of the X-ray source during image reconstruction from SECT measurements leads to so-called beam hardening artefacts which show as cupping and streaks. The reason is that the X-ray attenuation of any material is wavelength dependent. Thus the overall attenuation of an X-ray by an infinitesimal material volume depends on the spectral composition of the ray, which in turn depends on the types and amounts of materials the X-ray has already passed. Beam hardening artefacts can only be avoided by modelling the X-ray transmission for each wavelength separately and trying to identify the wavelength dependence of the attenuation at every location in the image to be reconstructed. This is a typical approach and also what will be encoded within our forward operator $\mathcal{I}$. However, identifying the wavelength dependence at a location is essentially equivalent to identifying the material composition, *i.e.* BHC actually requires some form of MD. It is therefore natural to tackle both BHC and MD simultaneously, which is why we take the volume fractions $\boldsymbol{w}$ of a predefined set of N_{mat} materials as our reconstruction variables.

Note that our regularization $R^{\alpha,\beta}$ contains a term that tries to enforce binary volume fractions, *i.e.* pure materials, which is in contrast to most existing approaches in BHC or MD and is motivated as follows: In general only one scalar field can be reconstructed from a SECT measurement (in the noisefree monochromatic setting this would be done by the inverse X-ray transform), for instance the (wavelength-averaged) attenuation coefficient or the spatially varying volume ratio in a mixture of two known materials. Volume fractions in mixtures of $N_{\mathrm{mat}} > 2$ materials are impossible to reconstruct, even if the mixture composition is identical everywhere: There is an $(N_{\mathrm{mat}}-1)$-dimensional manifold of compositions yielding the exact same measurement. (In contrast, in DECT or spectral CT the higher number of measurements would allow to reconstruct a higher number of variables.) By restricting to discrete, pure materials as we do, however, there is generically only a single material that fits the measurement (in essence, our sought unknown at each location is zero-dimensional). Theoretically one could also allow mixtures of up to two materials, but then these two materials must be known at each location: In monochromatic SECT the same attenuation coefficient can be obtained with any pair of materials (*via* judicious mixing of the two) as long as one has a stronger and the other a weaker attenuation, and even in the polychromatic setting the attenuation function (in the wavelength) of many materials lies in a two-dimensional space (spanned by the attenuation function due to the photoelectric effect and the attenuation function due to Compton scatter) in which the measurement fixes a one-dimensional submanifold that generically contains mixtures of many material pairs. We thus claim that without knowing for each location the two mixed materials beforehand, the only feasible approach to MD is by assuming pure materials at every location.

Of course, the above requires knowledge of which materials could occur. In most medical and industrial applications this is adequate; the only limitation is that the material number might become prohibitively high since mixtures such as alloys must explicitly be represented as a separate material (recall that our approach enforces pure materials). Also we simply ignore the fact that pixels or voxels at material interfaces are occupied by both neighbouring materials (incorporating this fact would require much more elaborate discretizations, but only marginally increase the image resolution).

A natural question is why one could not simply ignore the polychromaticity and then identify the materials from the reconstructed effective attenuations (in fact, this is often done in BHC). However, those attenuations may be very similar for two different materials so that the modelling error from ignoring polychromaticity already can impair the correct material choice (we will show some simulations where indeed nearby materials can be distinguished). Even more, the effective attenuation may be the same for two materials although the attenuation dependence on the wavelength is not. A polychromatic model like ours can then still decide which of the two materials fits better to the measured data since the different X-ray projections probe a large range of material thicknesses or equivalently wavelengths (recall that the effective attenuation coefficient at a location depends on the arriving wavelength spectrum and thus on the material thickness).

Note that our polychromatic forward operator $\mathcal{I}$ will require knowledge of the X-ray source spectrum. We believe this to be reasonable – it is certainly known to the scanner manufacturers and could even be determined experimentally by the user (which of course requires some effort, but is only done once).

As for our treatment of measurement noise, any CT measurement contains Poisson-distributed photon counting noise as well as Gaussian electronic noise or readout noise generated by CCD cameras [33,35]. Which one is dominant depends on the position in the sinogram due to the data dependency of Poisson noise. Nevertheless, practical reconstructions are often successful despite ignoring one or the other. However, if materials have to be distinguished based on differences in the wavelength dependence of the attenuation, then it is important to incorporate information from the whole spectrum and all material thicknesses and thus from regions where either noise dominates, which is why we model both.

In fact, the Poisson noise can only be correctly modelled if polychromaticity is taken into account, since CT uses energy detectors (compared to photon-counting detectors in PET) and the conversion of energy to photon number depends on the wavelength. Thus it is natural to combine BHC and MD from polychromaticity with a separation of Gaussian and Poisson noise.

Below we discuss the literature strands on BHC, MD, and noise modelling, which to our knowledge have not been combined before, in relation to our joint model.

1.2. Beam hardening correction

Beam hardening denotes the spectral shift to shorter wavelengths (higher photon energies) of a polychromatic X-ray passing through some material, which is due to a stronger attenuation at large wavelengths. It leads to a material thickness dependent effective attenuation and reconstruction artefacts if being ignored. Beam hardening can be reduced by so-called prefiltering (*i.e.* placing aluminium or copper in front of the X-ray source to narrow its spectrum). Alternatively, its nonlinear effect can be removed by measuring the X-ray projections separately for all wavelengths as in spectral CT or to some extent DECT (already suggested in the 70s). Without changing the scanner hardware there are essentially three approaches to avoid beam hardening artefacts: by regularization, by incorporating polychromaticity into the reconstruction model, and by learning.

Regularization (such as penalizing the total variation of the reconstruction) is used to counteract the ill-posedness of the reconstruction due to noise. If polychromaticity is ignored, this regularization additionally has to compensate for the corresponding modelling error – essentially this is the setting in all reconstructions based on approximately inverting the X-ray transform.

As for incorporating polychromaticity, if the scanned object consists just of a single material (as in some industrial applications), photon counts can readily be translated into material thickness (*e.g. via* lookup tables) so that standard X-ray inversion can be performed (note, though, that the corresponding nonlinear noise transformation is usually ignored) [34]. The extension to multiple materials is denoted linearization: Given an estimate of the material distribution, one calculates how the measurements with polychromatic and with monochromatic source would differ from each other and corrects the measurement by this difference to obtain a (hypothetical) monochromatic measurement, whose reconstruction does not show beam hardening artefacts. In the simplest case the estimated material distribution is just a single material (the most frequent) or a template with similar material distribution, in better cases it is obtained from a segmentation of a first uncorrected reconstruction [58]. This requires to know the material of each segmented part or to guess it just based on the reconstructed monochromatic attenuation (a variant is [51], who segment the reconstruction by correctly positioning known components such as surgical tools and only use a polychromatic model for those components). This is close to our approach, though with decisive differences: First, in our model the segmentation comes out of a joint optimization, and second, we do not define the material in a segmented region by its position in the segmentation or by the monochromatic attenuation (which may be the same for two different materials), but by the best fit to the global measurements.

Assuming only two materials, [21] improve on the linearization approach by simultaneously estimating the binary segmentation and the X-ray intensity loss as a function of the two material penetration thicknesses (modelled as a polynomial). Just like in our model, the segmentation is now part of the optimization just like the material (or rather its properties). In contrast to us they do not restrict to fixed materials, however, at the expense of only being able to deal with two materials.

A more accurate modelling, which can in principle also correctly account for the measurement noise, is to incorporate the full nonlinear polychromatic forward operator into the model (which is also what we suggest). This is done in [54], assuming that only two materials are present (typically bone and soft tissue) so that just the scalar volume ratio has to be reconstructed (Abella *et al.* [1] even manage without explicitly modelling the spectrum and wavelength-dependent attenuation coefficients; instead, their forward operator just maps the two material thicknesses along each ray to the measured photon count *via* a simple parametrized function with two experimentally chosen fitting parameters). Elbakri and Fessler [14] essentially consider the case where one material is air and the other material is known at each location, but may vary spatially. The reason why we can deal with more than two materials is our restriction to pure materials.

Instead of identifying the two materials one can exploit that the attenuation function (of the wavelength) of many materials in a certain X-ray range is a linear combination of two known basis functions (modelling attenuation due to the photoelectric effect and Compton scatter). In order to reconstruct the corresponding two linear coefficient fields from the scalar measurement, both are modelled as an explicit function of a scalar variable (*e.g.* the effective or the photoelectric attenuation coefficient [10,32]; another variant is [15], where the material mixture is taken as a function of the attenuation coefficient). We see two problems with this approach: First, it only works in a restricted range of the spectrum and only for materials without a K-edge (a sudden change in X-ray absorption at a material-specific wavelength due to photoelectric absorption [9], Chap. 5), which is why we instead choose the actual material distributions as our variable. Second, a one-to-one relation between the two linear coefficients is assumed which actually does not exist (unless all materials happen to lie on the same straight line in the two-dimensional attenuation function space).

As a simplification, [50,55] show that the wavelength spectrum actually only needs to be discretized by three bins if these are tuned appropriately. A complete circumvention of proper physical modelling is to just modify the monoenergetic forward operator by a heuristic of how the effective attenuation coefficient depends on all previous attenuation coefficients within the same ray, which can be parametrized by a few coefficients tuned by the user [4,29]. The additional tuning degrees of freedom of course allow to alleviate reconstruction artefacts for each reconstruction.

BHC *via* machine learning may in principle fall into either of the two previous categories: They might just regularize the reconstructions to look like previously seen images or they might actually learn a physics-based reconstruction model like ours. The latter is rather unlikely, though, as it is comparable to learning a notoriously difficult so-called end-to-end reconstruction, while learning image distributions already is standard in image processing. Kalare *et al.* [22] use a trained cascadic convolutional neural network (CNN) as a regularizer for removing artefacts after monoenergetic reconstructions, while [36] employ deep CNN within the reconstruction.

1.3. Material decomposition

We already noted that BHC often tries to identify the materials, which is termed MD in the CT community, only the goal is slightly different. Just like for BHC, one approach is to refine the measurement using DECT or spectral CT [31] (spectral CT may even be realized by DECT with dynamically changing energy threshold [56]; yet another technical alternative is phase contrast CT [11]). In principle, N_{mat} X-ray measurements at different wavelengths should allow to identify arbitrary mixture compositions of N_{mat} materials (even $N_{\mathrm{mat}}-1$ measurements suffice with the additional constraint that the volume fractions add up to one), though, as already explained previously, in some spectral and material ranges the space of attenuation functions is only two-dimensional so that more than two measurements might add no information. However, this is not true if the materials exhibit K-edges, allowing to distinguish more materials [46,49]. Typically variational methods are employed that can either already decompose the sinograms or the final reconstructed images into the different material components. Note that in our model we choose to decompose into different materials in the reconstructed image domain, since regularization in this domain is easier to interpret (for instance it is impossible to ensure pure materials on the sinogram level). The regularizations to get the material decomposition from the X-ray reconstructions at the different wavelengths include low-rank regularization (*via* the nuclear norm to ensure consistency of the images corresponding to different wavelengths) and sparsity regularization (*via* the

total variation, which we also use, to ensure piecwise homogeneous regions) [16]. Further prior knowledge can be the positivity of the material fractions (which we will also use) or the total mass of each material [19] (however, this mass is not known in many applications; furthermore, [19] treat the X-ray projections independently from each other). Machine learning may also help finetune variational MD with neural networks replacing the usual gradient descent steps [13].

Since we aim for MD without DECT or spectral CT, we have to exploit prior information instead. In the simplest case MD can already be performed for monochromatic CT measurements: After reconstruction one assigns each location a material based on the reconstructed attenuation coefficient. Xue *et al.* [52] even allow each pixel to be a mixture of two materials, which works well in experiments but is highly questionable since the same attenuation coefficient can be produced by mixing any two materials as long as one lies above and the other below. For exactly this reason we require pure materials. Xue *et al.* [53] slightly improve upon the model by adding a sparsity constraint that prefers a pure materials and a TV regularization, which is close to our approach apart from the monochromatic forward operator. The approaches in [27,59] are also questionable since they compute *via* a trained neural network a DECT from a SECT scan (the former then allows MD), this time for polychromatic SECT. This increases the dimension of the measurement data and the reconstruction – recall that for regularization and physical reasons we actually do the opposite and reduce the dimension of the reconstruction to a discrete number of materials! An alternative, physically reasonable approach is to augment the data by the information of the total object thickness at each sinogram location (which is sometimes known). Then indeed one can reconstruct (with a mono- as well as polychromatic spectrum) the volume ratio of two materials [23].

1.4. Noise reduction

Noise in transmission tomography is one of the main challenges for image reconstruction, especially in low-dose tomography. As mentioned before, Poisson-distributed photon counting noise and Gaussian electronic noise occur simultaneously. In monochromatic CT this can be statistically modelled *via* a mixed Poisson and Gaussian distribution [12,35]. In polychromatic CT the situation is more complicated: Rather than being Poisson distributed, the photon counting noise obeys a compound Poisson distribution [35].

A Bayesian ansatz is often used to develop a statistical reconstruction incorporating a noise model (in a data fidelity term) as well as prior knowledge about the reconstructed object (in a regularization term). For simplicity, most works just employ a pure Gaussian or pure Poisson noise model [20, 24, 28, 38, 45, 57]. The motivation for restricting to Gaussian noise is sometimes the electrical noise [36], but more often that it well approximates Poisson noise for high signal to noise ratios. However, its variance then would actually have to depend on the location in the sinogram. Due to the interdependence with MD as explained in the previous section, we explicitly model the Gaussian as well as the Poisson noise. Our corresponding data fidelity can be viewed as an extension of the data fidelity terms proposed initially in [6] and then adapted in [37] for monoenergetic CT reconstruction.

For regularization, most of the works previously cited employ a regularization *via* the total variation or variants of the so-called Huber loss of the image gradient. We will also adopt the total variation regularization in addition to a multiwell energy term which tries to enforce pure materials, as has been motivated and justified before (the term "multiwell" from the phase field literature refers to an integrand having multiple distinct local minimizers or "wells" – in our case at the pure materials).

1.5. Structure and notation

This paper is structured as follows. Section 2 stepwise motivates and derives all components of the objective functional (1.1) in detail before analysing it mathematically. To this end we start by detailing the forward operator $\mathcal{I}$ (modelling the photon energy dependent divergent beam transform) in Section 2.1 and present its mathematical properties. The variational model (1.1) will then be derived *via* a Bayesian ansatz in Section 2.2, and we conclude with Section 2.3 by proving its well-posedness, *i.e.* existence of minimizers, in Theorem 2.7. In Section 3 we propose an iterative scheme and detail all its algorithmic ingredients, closing the section with a

stability and convergence analysis. Finally, Section 4 presents numerical results on phantom data to illustrate the efficacy of our model and algorithm for polyenergetic CT measurements.

We will denote $\mathbb{R}^n$-valued quantities or functions by boldfont letters. The n-dimensional Lebesgue measure is denoted $\mathcal{L}^n$, the n-dimensional Hausdorff measure $\mathcal{H}^n$. For $p \in [1, \infty]$ the corresponding Lebesgue space on an open bounded domain Ω is denoted $L^p(\Omega)$, where sometimes we indicate a range R by $L^p(\Omega; R)$. The space of functions of bounded variation is denoted $\mathrm{BV}(\Omega)$ with corresponding total variation seminorm TV. Finally, the proximal operator of some function f on a Hilbert space X will be denoted by $\mathbf{prox}_f(x) = \operatorname{argmin}_{y \in X} \frac{1}{2}\|x - y\|_X^2 + f(y)$, and its Legendre–Fenchel conjugate by $f^*(y) = \sup_{x \in X} (x, y)_X - f(y)$, where $(\cdot, \cdot)_X$ and $\| \cdot \|_X$ denote the inner product and norm on X.

For the reader's convenience we furthermore here list the most important symbols used throughout the article as a reference.

$\Omega \subset \mathbb{R}^n$	Imaged region ($n = 2, 3$), p. 952
$\boldsymbol{\xi} \subset \mathbb{R}^n \setminus \overline{\Omega}$	Curve taken by X-ray source, p. 952
$\Sigma \subset \boldsymbol{\xi} \times \mathbb{S}^{n-1}$	Domain of sinogram, p. 952
$\mathcal{D}$	Divergent beam transform, p. 952
$[E_{\min}, E_{\max}]$	Range of X-ray source photon energies, p. 952
$I_0(E)$	Intensity of X-ray source as function of photon energy, p. 952
N_{mat}	Number of materials, p. 953
$\boldsymbol{g}(E) = (g_1(E), \dots, g_{N_{\mathrm{mat}}}(E))$	Energy-dependent attenuation coefficient for each material, p. 953
$\Delta \subset \mathbb{R}^{N_{\mathrm{mat}}}$	Probability simplex, p. 955
$\boldsymbol{w}(\boldsymbol{x}) = (w_1(\boldsymbol{x}), \dots, w_{N_{\mathrm{mat}}}(\boldsymbol{x})) \subset \Delta$	Sought material fractions at $\boldsymbol{x} \in \Omega$, p. 953
$\widetilde{\mathcal{I}}(u)(E, \cdot)$	Expected X-ray sinogram for photon energy E and spatially varying attenuation u, p. 953
$\widetilde{\mathcal{F}}(u)$	Polyenergetic CT forward operator or sinogram, *i.e.* integral of $\widetilde{\mathcal{I}}(u)(E, \cdot)$ over E, p. 953
$\mathcal{I}, \mathcal{F}$	Same as above, but operating on material density $\boldsymbol{w}$ rather than net attenuation u, p. 953
α, β	Regularization weights, p. 955
$R^{\alpha,\beta}$	Regularization functional, p. 955
R_1, R_2	Total variation and multiwell component of regularization functional, p. 955
d_{KL}	Generalized Kullback–Leibler divergence, p. 955
$f : \Sigma \to \mathbb{R}$	Measured noisy sinogram, p. 954
$\sigma > 0$	Standard deviation of Gaussian detector readout noise, p. 954
$y : \Sigma \to [0, \infty)$	Sought photon density, p. 954
$F(y, \boldsymbol{w})$	Objective functional, *i.e.* negative log-posterior, p. 956
$W_0 : [0, \infty) \to [0, \infty)$	Lambert-W function, *i.e.* inverse of $z \mapsto z \exp z$, p. 956
$y_{\boldsymbol{w}}, Y_{\boldsymbol{w}}$	Minimizer of $F(\cdot, \boldsymbol{w})$ and its integral over $[E_{\min}, E_{\max}]$, p. 956
$y^k, \boldsymbol{w}^k$	Iterates of the iterative algorithm, p. 958
ζ_k	Damping parameter of iterative algorithm, p. 959
ε	Regularization parameter of iterative algorithm to ensure positivity, p. 958
G, A_k^ε, C_k	Algorithmic quantities of each iteration for convergence analysis, p. 961

2. A variational model for multimaterial polyenergetic CT reconstruction

This section presents, motivates and briefly analyses the variational model we propose.

2.1. The polyenergetic CT forward operator

We briefly recapitulate the polyenergetic CT forward operator. The imaged sample is supposed to lie in the bounded open domain $\Omega \subset \mathbb{R}^n$ $(n = 2, 3)$. In practical X-ray CT the pointlike X-ray source is moved around the sample along a smooth curve $\boldsymbol{\xi} \subset \mathbb{R}^n \setminus \overline{\Omega}$ of finite length and without self-intersections. When the source is at position $\boldsymbol{x} \in \boldsymbol{\xi}$, the X-rays emanating from it in direction $\boldsymbol{\theta} \subset \mathbb{S}^{n-1}$ correspond to the half line

$$L^+_{\boldsymbol{x},\boldsymbol{\theta}} := \{\boldsymbol{x} + s\boldsymbol{\theta} : \ s \in [0, \infty)\}.$$

The X-ray intensity transmitted through Ω along each half line is recorded, thus we have a measurement for every point in $\boldsymbol{\xi} \times \mathbb{S}^{n-1}$, where without loss of generality we may also reduce $\boldsymbol{\xi} \times \mathbb{S}^{n-1}$ to

$$\Sigma = \{(\boldsymbol{x}, \boldsymbol{\theta}) \in \boldsymbol{\xi} \times \mathbb{S}^{n-1} : \ \mathcal{H}^1(L^+_{\boldsymbol{x},\boldsymbol{\theta}} \cap \Omega) > 0\},$$

equipped with the n-dimensional Hausdorff measure $\mathcal{H}^n$. The associated linear operator is the so-called divergent X-ray transform [30], also known as fan- or cone-beam transform in two and three space dimensions, respectively.

Definition 2.1 (Divergent X-ray transform)**.** The divergent X-ray transform is the bounded linear operator $\mathcal{D} : L^q(\Omega) \to L^q(\Sigma)$ for $q \in [1, \infty]$ defined by

$$\mathcal{D}u(\boldsymbol{x}, \boldsymbol{\theta}) = \int_{L^+_{\boldsymbol{x},\boldsymbol{\theta}}} u(\boldsymbol{z}) \, \mathrm{d}\mathcal{H}^1(\boldsymbol{z}). \tag{2.1}$$

The following properties are straightforward to check.

Lemma 2.2 (Properties of $\mathcal{D}$)**.**

(1) *The adjoint operator $\mathcal{D}^* : L^{q'}(\Sigma) \to L^{q'}(\Omega)$ to $\mathcal{D}$ with $q' = \frac{q}{q-1}$ is given by (see e.g. [18], Cor. 3.16)*

$$\mathcal{D}^* w(\boldsymbol{z}) = \int_{\boldsymbol{\xi}} |\boldsymbol{z} - \boldsymbol{x}|^{1-n} w\left(\boldsymbol{x}, \frac{\boldsymbol{z} - \boldsymbol{x}}{|\boldsymbol{z} - \boldsymbol{x}|}\right) \mathrm{d}\mathcal{H}^1(\boldsymbol{x}). \tag{2.2}$$

(2) *The operator $\mathcal{D}$ preserves positivity, i.e. $\mathcal{D}u \geq 0$ for any $u \geq 0$.*
(3) *The divergent beam transform $\mathcal{D}$ is also bounded as an operator from $L^\infty(\Omega)$ to $L^\infty(\Sigma)$ with norm no larger than the diameter of Ω.*
(4) *The operator $\mathcal{D}$ does not annihilate constant functions, i.e. $\mathcal{D}\mathbf{1}_\Omega \neq 0$.*

When passing through a material, an X-ray is attenuated. The amount of attenuation at each point is quantified by the (spatially varying, material-dependent) attenuation coefficient $u : \Omega \to [0, \infty)$. By Beer's law the energy fraction passing through the material without being absorbed (the so-called transmittance) equals $\exp(-U)$ for $U = \int_{L^+_{\boldsymbol{x},\boldsymbol{\theta}}} u(x) \, \mathrm{d}\mathcal{H}^1$ the accumulated attenuation coefficient along the ray. However, this formula only holds for monochromatic or monoenergetic X-rays, since the attenuation coefficient of a material also depends on the X-ray wavelength. Practical X-ray sources are polyenergetic, *i.e.* they emit a continuous spectrum of wavelengths, described by an integrable function

$$I_0 : [E_{\min}, E_{\max}] \to [0, \infty)$$

that indicates the intensity or amount of X-rays emitted at each wavelength (rather than the wavelength, the argument of I_0 is the energy of a photon, which is in one-to-one correspondence with the photon's wavelength and lies between a minimum and a maximum possible energy $E_{\min}$ and $E_{\max}$). Thus, if $u : \Omega \times [E_{\min}, E_{\max}] \to [0, \infty)$ describes the attenuation coefficient as a function of spatial position and photon energy, the expected number of photons or X-ray intensity passing through the material is expressed by the following polyenergetic CT forward operator.

Definition 2.3 (Polyenergetic CT forward operator)**.** The *expected X-ray intensity* resulting from a Lebesgue measurable $u : \Omega \times [E_{\min}, E_{\max}] \to [0, \infty)$ is defined for $\mathcal{L}^1 \otimes \mathcal{H}^n$-almost all $(E, \boldsymbol{x}, \boldsymbol{\theta}) \in [E_{\min}, E_{\max}] \times \Sigma$ *via*

$$\widetilde{\mathcal{I}}(u)(E, \boldsymbol{x}, \boldsymbol{\theta}) = I_0(E) \exp(-\mathcal{D}u(\boldsymbol{x}, \boldsymbol{\theta}, E)),$$

where for each $E > 0$ we write $\mathcal{D}u(\boldsymbol{x}, \boldsymbol{\theta}, E)$ for $\mathcal{D}(u(\cdot, E))$ evaluated at $(\boldsymbol{x}, \boldsymbol{\theta})$. The *polyenergetic CT forward operator* then is

$$\widetilde{\mathcal{F}}(u)(\boldsymbol{x}, \boldsymbol{\theta}) = \int_{E_{\min}}^{E_{\max}} \widetilde{\mathcal{I}}(u)(E, \boldsymbol{x}, \boldsymbol{\theta}) \, \mathrm{d}\mathcal{L}^1(E) = \int_{E_{\min}}^{E_{\max}} I_0(E) \exp(-\mathcal{D}u(\boldsymbol{x}, \boldsymbol{\theta}, E)) \, \mathrm{d}\mathcal{L}^1(E).$$

Since in the above forward operator the transmittance is accumulated over all photon energies (unlike in spectral CT, where photons at different wavelengths are distinguished in the measurement), it is impossible to reconstruct the energy dependence of the attenuation coefficient u. Therefore, the use of the polyenergetic CT forward operator only makes sense in combination with further prior knowledge. We will assume that the scanned object consists of N_{mat} different materials with known, bounded photon energy dependent attenuation coefficients

$$g_i : [E_{\min}, E_{\max}] \to [0, \infty), \quad i = 1, \dots, N_{\mathrm{mat}}$$

as they can for instance be found in www.nist.gov/pml/data/xraycoef/. We will write $\boldsymbol{g} = (g_1, \dots, g_{N_{\mathrm{mat}}})$. The attenuation coefficient of the sample can then be expressed as

$$u(\boldsymbol{z}, E) = \sum_{i=1}^{N_{\mathrm{mat}}} g_i(E) w_i(\boldsymbol{z}) \tag{2.3}$$

with $w_i : \Omega \to [0, 1]$ the spatial distribution of the ith material, indicating at each point its volume proportion. Including void as one of the materials, all volume proportions have to add up to one,

$$\sum_{i=1}^{N_{\mathrm{mat}}} w_i = 1.$$

Summarizing, the expected intensity of X-rays passing through the sample can be expressed in terms of the unknown material distributions $\boldsymbol{w} = (w_1, \dots, w_{N_{\mathrm{mat}}})$ as

$$\mathcal{I}(\boldsymbol{w})(E, \boldsymbol{x}, \boldsymbol{\theta}) = \widetilde{\mathcal{I}}(u)(E, \boldsymbol{x}, \boldsymbol{\theta}) = I_0(E) \exp\left(- \sum_{i=1}^{N_{\mathrm{mat}}} g_i(E) \mathcal{D}w_i(\boldsymbol{x}, \boldsymbol{\theta}) \right),$$

and we aim to reconstruct $\boldsymbol{w}$ from a measurement of

$$\mathcal{F}(\boldsymbol{w}) = \widetilde{\mathcal{F}}(u) = \int_{E_{\min}}^{E_{\max}} I_0(E) \exp\left(- \sum_{i=1}^{N_{\mathrm{mat}}} g_i(E) \mathcal{D}w_i \right) \mathrm{d}\mathcal{L}^1(E). \tag{2.4}$$

Lemma 2.4 (L^1-continuity of $\mathcal{I}$ and $\mathcal{F}$)**.** *The operator $\mathcal{I}$ is continuous from $L^1(\Omega; [0, 1]^{N_{\mathrm{mat}}})$ to $L^1((E_{\min}, E_{\max}) \times \Sigma)$, the operator $\mathcal{F}$ is continuous from $L^1(\Omega; [0, 1]^{N_{\mathrm{mat}}})$ to $L^1(\Sigma)$.*

Proof. Since $w_i, g_i \geq 0$ for all i we have $\exp\left(- \sum_{i=1}^{N_{\mathrm{mat}}} g_i(E) \mathcal{D}w_i \right) \in [0, 1]$ and thus

$$|\mathcal{I}(\boldsymbol{w})(E, \boldsymbol{x}, \boldsymbol{\theta})| \leq I_0(E) \qquad \text{and} \qquad |\mathcal{F}(\boldsymbol{w})| \leq \int_{E_{\min}}^{E_{\max}} I_0(E) \, \mathrm{d}\mathcal{L}^1(E)$$

so that $\mathfrak{I}$ indeed maps into $L^1((E_{\min}, E_{\max})\times\Sigma)$ and $\mathcal{F}$ even maps into $L^\infty(\Sigma)$. Furthermore, due to the Lipschitz continuity of exp on $(-\infty, 0]$ with Lipschitz constant 1 we have

$$\begin{aligned}|\mathfrak{I}(\boldsymbol{w}) - \mathfrak{I}(\tilde{\boldsymbol{w}})| &= I_0(E)\left|\exp\left(-\sum_{i=1}^{N_{\mathrm{mat}}} g_i(E)\mathcal{D}w_i\right) - \exp\left(-\sum_{i=1}^{N_{\mathrm{mat}}} g_i(E)\mathcal{D}\tilde{w}_i\right)\right| \\ &\le I_0(E)\sum_{i=1}^{N_{\mathrm{mat}}} g_i(E)|\mathcal{D}w_i - \mathcal{D}\tilde{w}_i| \le \max_i(I_0(E)g_i(E))\sum_{i=1}^{N_{\mathrm{mat}}}|\mathcal{D}w_i - \mathcal{D}\tilde{w}_i|.\end{aligned}$$

Integrating over $(E_{\min}, E_{\max})\times\Sigma$, the continuity statement for $\mathfrak{I}$ then follows from the L^1-continuity of $\mathcal{D}$. The L^1-continuity of $\mathcal{F}$ now is a direct consequence due to $\|\mathcal{F}(\boldsymbol{w}) - \mathcal{F}(\tilde{\boldsymbol{w}})\|_{L^1(\Sigma)} = \left\|\int_{E_{\min}}^{E_{\max}} \mathfrak{I}(\boldsymbol{w}) - \mathfrak{I}(\tilde{\boldsymbol{w}})\,\mathrm{d}\mathcal{L}^1\right\|_{L^1(\Sigma)} \le \|\mathfrak{I}(\boldsymbol{w}) - \mathfrak{I}(\tilde{\boldsymbol{w}})\|_{L^1((E_{\min},E_{\max})\times\Sigma)}$. □

2.2. Bayesian motivation of the variational reconstruction

We now briefly motivate our variational approach for the CT reconstruction from a Bayesian perspective, following [6,26,37]. The quantity $\mathcal{F}(\boldsymbol{w})(\boldsymbol{x},\boldsymbol{\theta})$ from (2.4) in fact only represents the expected intensity of X-rays passing through the sample along the ray defined by $(\boldsymbol{x},\boldsymbol{\theta})$. The actual number of arriving photons, though, which is the measured quantity, is governed by a Poisson process with that intensity. In addition, the photons are typically counted with charged coupled devices (CCD) that exhibit Gaussian background noise [30,33]. We aim to account for both types of noise.

Let the domain Σ of the measurement be partitioned into detectors D_i (in fact, in a real CT system the physical detectors are moved along with the X-ray source, so each D_i corresponds to a true physical detector, representing a subset of $\mathbb{S}^{n-1}$, times a segment of the curve $\boldsymbol{\xi}$ corresponding to a measurement time interval during the motion). Similarly, let the energy interval $[E_{\min}, E_{\max}]$ be partitioned into subintervals E_i. The expected number of photons from energy range E_i arriving at detector D_j is then given by

$$\bar{y}_{ij}(\boldsymbol{w}) = \int_{E_i}\int_{D_j} \mathfrak{I}(\boldsymbol{w})(E,\boldsymbol{x},\boldsymbol{\theta})\,\mathrm{d}\mathcal{H}^n(\boldsymbol{x},\boldsymbol{\theta})\,\mathrm{d}\mathcal{L}^1(E).$$

The actual number of photons y_{ij} then is a Poisson-distributed random variable with mean $\bar{y}_{ij}(\boldsymbol{w})$,

$$y_{ij} \sim \mathcal{P}(\bar{y}_{ij}(\boldsymbol{w})),$$

and the actual measurement, the readout f_j of detector D_j, will be the total number of photons, summed over all energy ranges and perturbed by normally distributed noise, thus

$$f_j \sim \mathcal{N}\big(\textstyle\sum_i y_{ij}, \mathcal{H}^n(D_j)\sigma^2\big),$$

where σ^2 denotes the (usually known) noise variance per detector area. Note that since the noise of all CCDs within a detector D_j is independent, the noise variance of the detector is the sum of the noise variances of each CCD by the Bienaymé formula, and since the number of CCDs is proportional to the detector area, so must be the noise variance.

The quantities $f = (f_j)_j$ and $y = (y_{ij})_{ij}$ are stochastic variables, whose distribution depends on $\bar{y}(\boldsymbol{w}) = (\bar{y}_{ij}(\boldsymbol{w}))_{ij}$ and thus on $\boldsymbol{w}$. Denoting by $\pi(y, \bar{y}(\boldsymbol{w})|f)$ the probability density of true photon numbers y and expected intensity $\bar{y}(\boldsymbol{w})$ given the measurement f, the maximum *a posteriori* (MAP) estimate tries to identify y and $\bar{y}(\boldsymbol{w})$ or rather $\boldsymbol{w}$ as the configuration $(y^*, \boldsymbol{w}^*)$ with highest probability,

$$(y^*, \boldsymbol{w}^*) = \operatorname{argmax}\pi(y, \bar{y}(\boldsymbol{w})|f) = \operatorname{argmin} -\log\pi(y, \bar{y}(\boldsymbol{w})|f).$$

By Bayes' rule,

$$\pi(y, \bar{y}(\boldsymbol{w})|f) = \frac{\pi(y, \bar{y}(\boldsymbol{w}), f)}{\pi(f)} = \frac{\pi(y, \bar{y}(\boldsymbol{w}), f)}{\pi(y, \bar{y}(\boldsymbol{w}))}\,\frac{\pi(y, \bar{y}(\boldsymbol{w}))}{\pi(\bar{y}(\boldsymbol{w}))}\,\frac{\pi(\bar{y}(\boldsymbol{w}))}{\pi(f)}$$

$$= \frac{\pi(f|y,\bar{y}(\boldsymbol{w}))\pi(y|\bar{y}(\boldsymbol{w}))\pi(\bar{y}(\boldsymbol{w}))}{\pi(f)}.$$

Due to the above assumptions on the distributions we can explicitly express two of the probability densities,

$$\pi(f|y,\bar{y}(\boldsymbol{w})) = \prod_j \pi(f_j|(y_{ij})_i) = \prod_j \frac{1}{\sqrt{2\pi\mathcal{H}^n(D_j)}\sigma} \exp\left(-\frac{1}{2\mathcal{H}^n(D_j)\sigma^2}\left(f_j - \sum_i y_{ij}\right)^2\right),$$
$$\pi(y|\bar{y}(\boldsymbol{w})) = \prod_{i,j} \pi(y_{ij}|\bar{y}_{ij}(\boldsymbol{w})) = \prod_{i,j} \frac{\bar{y}_{ij}(\boldsymbol{w})^{y_{ij}} e^{-\bar{y}_{ij}(\boldsymbol{w})}}{y_{ij}!}.$$

Furthermore, as is frequently done, for the prior density $\pi(\bar{y}(\boldsymbol{w}))$ we will assume a Gibbs distribution of the form

$$\pi(\bar{y}(\boldsymbol{w})) = \pi(\boldsymbol{w}) = \frac{1}{Z}\exp(-R^{\alpha,\beta}(\boldsymbol{w}))$$

with Z a normalization constant and $R^{\alpha,\beta}$ a regularization functional depending on nonnegative tuning weights $\alpha, \beta \geq 0$. Material distributions with lower values of $R^{\alpha,\beta}$ are thus assigned a higher probability. Abbreviating the probability simplex as

$$\Delta = \left\{ \boldsymbol{w} \in \mathbb{R}^{N_{\mathrm{mat}}} \,\middle|\, w_1, \ldots, w_{N_{\mathrm{mat}}} \geq 0,\ \sum_{i=1}^{N_{\mathrm{mat}}} w_i = 1 \right\},$$

we choose

$$R^{\alpha,\beta}(\boldsymbol{w}) = \alpha R_1(\boldsymbol{w}) + \beta R_2(\boldsymbol{w}) \quad \text{with} \begin{cases} R_1(\boldsymbol{w}) = \sum_{i=1}^{N_{\mathrm{mat}}} \mathrm{TV}(w_i) + \int_\Omega \iota_\Delta(\boldsymbol{w})\,\mathrm{d}\mathcal{L}^n \text{ and} \\ R_2(\boldsymbol{w}) = -\frac{1}{2}\int_\Omega |\boldsymbol{w} - \mathbf{1}/N_{\mathrm{mat}}|^2\,\mathrm{d}\mathcal{L}^n. \end{cases}$$

Above, $\mathbf{1}$ represents the vector of ones, ι_Δ is the convex indicator function of the probability simplex, and TV is the total variation seminorm. The total variation term in R_1 is known to prefer spatially piecewise constant material densities, while the quadratic term R_2 is minimal at pure materials (hence sometimes termed a "multiwell") and thus prefers these.

Remark 2.5 (Alternative multiwell)**.** An alternative multiwell choice would have been the entropy $-\int_\Omega \sum_{i=1}^{N_{\mathrm{mat}}} w_i \log w_i\,\mathrm{d}\mathcal{L}^n$, which qualitatively differs from the above quadratic term in that its slope at the pure materials diverges, hence providing an even stronger incentive for pure materials. For this very reason, however, such a multiwell would no longer be Gâteaux or directionally differentiable in any Lebesgue space (since in a pure material region the derivative is unbounded) so that we refrain from this choice. Numerically this deficiency would manifest as difficulties in the optimization: Subsets of Ω could get locked in pure material phases from which the optimization cannot escape.

Summarizing, if in $-\log\pi(y,\bar{y}(\boldsymbol{w})|f)$ we ignore terms independent of $(y,\boldsymbol{w})$ (which we will generally do in the following as they have no influence on the minimizer), the MAP estimate is obtained as minimizer $(y,\boldsymbol{w})$ of

$$\sum_j \frac{1}{2\mathcal{H}^n(D_j)\sigma^2}\left(f_j - \sum_i y_{ij}\right)^2 + \sum_{i,j}(\log y_{ij}! + \bar{y}_{ij}(\boldsymbol{w}) - y_{ij}\log\bar{y}_{ij}(\boldsymbol{w})) + R^{\alpha,\beta}(\boldsymbol{w}).$$

With the Stirling approximation $\log(n!) = n\log(n) - n + O(\log(n))$ as $n \to \infty$ and the generalized Kullback–Leibler divergence

$$d_{\mathrm{KL}}(z,\bar{z}) = \begin{cases} z\log(\frac{z}{\bar{z}}) - z + \bar{z} & \text{if } z,\bar{z} \geq 0 \\ \infty & \text{else} \end{cases}$$

(using the formal convention $\frac{1}{0} = \infty$, $\frac{0}{0} = 1$, and $0 \log 0 = 0$) this becomes

$$\sum_j \frac{1}{2\mathcal{H}^n(D_j)\sigma^2} \left(f_j - \sum_i y_{ij} \right)^2 + \sum_{i,j} d_{\mathrm{KL}}(y_{ij}, \bar{y}_{ij}(\boldsymbol{w})) + R^{\alpha,\beta}(\boldsymbol{w}).$$

Now identify the vectors f and y with piecewise constant functions $f : \Sigma \to \mathbb{R}$ and $y : [E_{\min}, E_{\max}] \times \Sigma \to \mathbb{R}$ (with a slight misuse of notation we use the same symbol) such that

$$f = \frac{f_j}{\mathcal{H}^n(D_j)} \text{ on detector } D_j, \qquad y = \frac{y_{ij}}{\mathcal{L}^1(E_i)\mathcal{H}^n(D_j)} \text{ on } E_i \times D_j$$

(thus f_j and y_{ij} are the accumulated values of f on D_j and y on $E_i \times D_j$). Furthermore note that under sufficient regularity of $\boldsymbol{w}$ (for instance $\boldsymbol{w}$ with strictly convex level lines) the intensity $\mathcal{I}(\boldsymbol{w})$ is continuous so that $\mathcal{I}(\boldsymbol{w}) \approx \frac{\bar{y}_{ij}(\boldsymbol{w})}{\mathcal{L}^1(E_i)\mathcal{H}^n(D_j)}$ on $E_i \times D_j$. With this approximation the above energy now reads

$$F(y, \boldsymbol{w}) = \frac{1}{2\sigma^2} \int_\Sigma \left(f - \int_{E_{\min}}^{E_{\max}} y \, \mathrm{d}\mathcal{L}^1 \right)^2 \mathrm{d}\mathcal{H}^n + \int_\Sigma \int_{E_{\min}}^{E_{\max}} d_{\mathrm{KL}}(y, \mathcal{I}(\boldsymbol{w})) \, \mathrm{d}\mathcal{L}^1 \, \mathrm{d}\mathcal{H}^n + R^{\alpha,\beta}(\boldsymbol{w}).$$

Therefore, we will define our CT-reconstruction from the measurement f as a minimizer of this energy F (where we no longer require y to be piecewise constant). We remark that the last transition from discrete detectors to the continuum setting has been merely formal, but could be made rigorous in form of a Γ-convergence result, showing that minimizers of the functional with discrete detectors converge to minimizers of F as the size of the detectors and distinguished energy ranges uniformly tends to zero.

2.3. Well-posedness analysis

We briefly prove existence of minimizers for our reconstruction functional F. Note that F is in general not convex so that uniqueness of minimizers cannot be expected: Indeed, the β-weighted regularization term in $R^{\alpha,\beta}$ is purposely designed to have different local minima exactly at the pure material distributions. Furthermore, even though the Kullback–Leibler divergence is convex, its composition with the nonlinear operator $\mathcal{I}$ no longer is, as can easily be seen from $(y, s) \mapsto d_{\mathrm{KL}}(y, I_0(E)\exp(-s))$ having Hessian

$$\begin{pmatrix} 1/y & 1 \\ 1 & I_0(E)\exp(-s) \end{pmatrix},$$

which may become indefinite for large y or s. Another consequence of the nonconvexity is that for existence of minimizers strong compactness in L^1 will be required of material distributions with finite cost F. This strong compactness is provided by the total variation seminorm within the regularizer $R^{\alpha,\beta}$, without which the reconstruction problem would not be well-posed. We will exploit that for given $\boldsymbol{w}$ the optimal y can be explicitly computed.

Lemma 2.6 (Minimizing photon count)**.** *For any $f \in L^2(\Sigma)$ and $\boldsymbol{w} \in (L^\infty(\Omega))^{N_{\mathrm{mat}}}$ the minimizer $y_{\boldsymbol{w}}$ of $F(\cdot, \boldsymbol{w})$ can be explicitly computed pointwise. Indeed, abbreviating $Y_{\boldsymbol{w}} = \int_{E_{\min}}^{E_{\max}} y_{\boldsymbol{w}} \, \mathrm{d}\mathcal{L}^1$, the functions $y_{\boldsymbol{w}}$ and $Y_{\boldsymbol{w}}$ satisfy*

$$\begin{aligned} y_{\boldsymbol{w}} &= \mathcal{I}(\boldsymbol{w}) \exp\left(\tfrac{f - Y_{\boldsymbol{w}}}{\sigma^2} \right), \\ Y_{\boldsymbol{w}} &= \mathcal{F}(\boldsymbol{w}) \exp\left(\tfrac{f - Y_{\boldsymbol{w}}}{\sigma^2} \right) \\ &= \sigma^2 W_0\left(\tfrac{1}{\sigma^2} \mathcal{F}(\boldsymbol{w}) \exp\left(\tfrac{f}{\sigma^2} \right) \right) \end{aligned}$$

for W_0 the Lambert-W function which is the inverse of $z \mapsto z\exp(z)$ (cf. [3]).

Proof. The functional F is strictly convex in y. Thus it suffices to solve the first order optimality condition

$$\begin{aligned} 0 = \partial_y F(y_{\boldsymbol{w}}, \boldsymbol{w}) &= \frac{1}{\sigma^2}\left(\int_{E_{\min}}^{E_{\max}} y_{\boldsymbol{w}} \,\mathrm{d}\mathcal{L}^1 - f\right) + \log \frac{y_{\boldsymbol{w}}}{\mathfrak{I}(\boldsymbol{w})} \\ &= \frac{1}{\sigma^2}(Y_{\boldsymbol{w}} - f) + \log \frac{y_{\boldsymbol{w}}}{\mathfrak{I}(\boldsymbol{w})}, \end{aligned}$$

which yields the first equation. Integrating both sides of that equation over $[E_{\min}, E_{\max}]$ and using $\mathcal{F}(\boldsymbol{w}) = \int_{E_{\min}}^{E_{\max}} \mathfrak{I}(\boldsymbol{w}) \,\mathrm{d}\mathcal{L}^1$ yields the second equation. Multiplying that second equation by $\frac{1}{\sigma^2}\exp\frac{Y_{\boldsymbol{w}}}{\sigma^2}$ yields

$$\frac{Y_{\boldsymbol{w}}}{\sigma^2}\exp\frac{Y_{\boldsymbol{w}}}{\sigma^2} = \frac{1}{\sigma^2}\mathcal{F}(\boldsymbol{w})\exp\left(\frac{f}{\sigma^2}\right)$$

so that indeed $Y_{\boldsymbol{w}} = \sigma^2 W_0\big(\frac{1}{\sigma^2}\mathcal{F}(\boldsymbol{w})\exp\big(\frac{f}{\sigma^2}\big)\big)$. □

Now we can show existence of minimizers for F.

Theorem 2.7 (Existence of minimizers)**.** *For any $f \in L^2(\Sigma)$ there exists a minimizer $(y, \boldsymbol{w}) \in L^\infty((E_{\min}, E_{\max}) \times \Sigma) \times (\mathrm{BV}(\Omega))^{N_{\mathrm{mat}}}$ of F with finite $F(y, \boldsymbol{w})$.*

Proof. We follow the standard direct method of the calculus of variations. The choice $y = 0$, $w_1 = 1$, $w_2 = \cdots = w_{N_{\mathrm{mat}}} = 0$ satisfies $F(y, \boldsymbol{w}) = \frac{1}{2\sigma^2}\|f\|_{L^2}^2 + \int_\Sigma \int_{E_{\max}}^{E_{\min}} \mathfrak{I}(\boldsymbol{w}) \,\mathrm{d}\mathcal{L}^1 \,\mathrm{d}\mathcal{H}^n + \beta R_2(\boldsymbol{w}) < \infty$ so that F is proper. Furthermore, since $d_{\mathrm{KL}} \geq 0$ we have $F(y, \boldsymbol{w}) \geq -\beta\mathcal{L}^n(\Omega)(N_{\mathrm{mat}} - 1)/(2N_{\mathrm{mat}})$ so that F is bounded from below.

Now consider a minimizing sequence $(y^n, \boldsymbol{w}^n)$, $n = 1, 2, \ldots$, such that $F(y^n, \boldsymbol{w}^n)$ converges monotonically to $\inf F$. Without loss of generality we may assume $F(y^1, \boldsymbol{w}^1) < \infty$ so that for all n we have $w_1^n, \ldots, w_{N_{\mathrm{mat}}}^n \geq 0$ with $w_1^n + \cdots + w_{N_{\mathrm{mat}}}^n = 1$ almost everywhere (otherwise $R^{\alpha,\beta}$ would be infinite). Furthermore we may assume $y^n = y_{\boldsymbol{w}^n}$ to be the optimal photon count from Lemma 2.6.

Since $\alpha\mathrm{TV}(w_i^n)$ is part of F, all $w_1^n, \ldots, w_{N_{\mathrm{mat}}}^n$ are uniformly bounded in $\mathrm{BV}(\Omega)$ so that there exists a weakly-*converging subsequence $\boldsymbol{w}^n \overset{*}{\rightharpoonup} \overline{\boldsymbol{w}}$ in $(\mathrm{BV}(\Omega))^{N_{\mathrm{mat}}}$, which for simplicity we again index by n. By the compact embedding of BV into L^1 we also have strong convergence in $L^1(\Omega)$ and thus by Lemma 2.4 that $\mathfrak{I}(\boldsymbol{w}^n) \to \mathfrak{I}(\overline{\boldsymbol{w}})$ in $L^1((E_{\min}, E_{\max}) \times \Sigma)$ and $\mathcal{F}(\boldsymbol{w}^n) \to \mathcal{F}(\overline{\boldsymbol{w}})$ in $L^1(\Sigma)$. After extracting a further subsequence we may in both cases even assume pointwise convergence almost everywhere. Lemma 2.6 then implies pointwise convergence almost everywhere of $Y_{\boldsymbol{w}^n}$ and $y^n = y_{\boldsymbol{w}^n}$ to $Y_{\overline{\boldsymbol{w}}}$ and $\bar{y} = y_{\overline{\boldsymbol{w}}}$. We thus obtain

$$\begin{aligned} \lim_{n\to\infty} F(y^n, \boldsymbol{w}^n) = \lim_{n\to\infty} \frac{1}{2\sigma^2}\int_\Sigma (f - Y_{\boldsymbol{w}^n})^2 \,\mathrm{d}\mathcal{H}^n + \int_\Sigma \int_{E_{\min}}^{E_{\max}} d_{\mathrm{KL}}(y_{\boldsymbol{w}^n}, \mathfrak{I}(\boldsymbol{w}^n)) \,\mathrm{d}\mathcal{L}^1 \,\mathrm{d}\mathcal{H}^n \\ + \alpha \sum_{i=1}^{N_{\mathrm{mat}}} \mathrm{TV}(w_i^n) + \frac{\beta}{2}\int_\Omega -|\boldsymbol{w}^n - \mathbf{1}/N_{\mathrm{mat}}|^2 \,\mathrm{d}\mathcal{L}^n \geq F(y_{\overline{\boldsymbol{w}}}, \overline{\boldsymbol{w}}), \end{aligned}$$

where the last inequality follows from the sequential lower semi-continuity of TV with respect to weak-*convergence in BV and from Fatou's lemma since all integrands are lower semi-continuous and uniformly bounded from below. Thus a minimizer is given by $(y_{\overline{\boldsymbol{w}}}, \overline{\boldsymbol{w}})$. □

3. An alternating minimization with forward backward splitting

We here present an alternating minimization alorithm for y and $\boldsymbol{w}$ in which the minimization of $\boldsymbol{w}$ is of forward backward splitting type. The scheme is provably convergent and, through an update similar to expectation maximization in emission tomography, quickly reaches material distributions more or less consistent with the measurements. The three-step iterative scheme is summarized in Algorithm 1; its three steps are explained in the next and further algorithmic details in the subsequent paragraphs.

Note that we will also provide two alternative schemes in the appendix in Sections A and B that may be more efficient in the regime of low regularization.

Algorithm 1. Iterative algorithm for polyenergetic CT reconstruction.

initialize $y^0, \boldsymbol{w}^0$
for $k = 1, \dots$ **do**
  calculate y^k by explicitly minimizing $F(\cdot, \boldsymbol{w}^{k-1})$, see (3.1)
  perform a forward step in $\boldsymbol{w}$, yielding $w^{\varepsilon}_{i,y^k}(\boldsymbol{w}^{k-1})$ for $i = 1, \dots, N_{\mathrm{mat}}$, see (3.3)
  perform a regularization step in $\boldsymbol{w}$, yielding $\boldsymbol{w}^k$, see (3.5)
  if reinitialization condition **then**
    run a reinitialization heuristic (see Sect. 3.4) to avoid spurious local minima
  end if
end for

3.1. Alternation and forward backward splitting

In the kth iteration of Algorithm 1 we first minimize for y with $\boldsymbol{w}$ fixed, which by Lemma 2.6 yields

$$\begin{aligned} y^k &= \mathfrak{I}(\boldsymbol{w}^{k-1}) \exp\left(\tfrac{f}{\sigma^2} - W_0\left(\frac{\mathcal{F}(\boldsymbol{w}^{k-1})}{\sigma^2} \exp\left(\tfrac{f}{\sigma^2}\right)\right)\right) \\ &= \mathfrak{I}(\boldsymbol{w}^{k-1}) \frac{W_0\left(\frac{\mathcal{F}(\boldsymbol{w}^{k-1})}{\sigma^2} \exp\left(\frac{f}{\sigma^2}\right)\right)}{\mathcal{F}(\boldsymbol{w}^{k-1})/\sigma^2}, \end{aligned} \tag{3.1}$$

where we used the identity $\exp(-W_0(z)) = W_0(z)/z$. Then we fix y to the value y^k and perform one minimization step for $\boldsymbol{w}$. To this end we first calculate the first order necessary optimality condition for minimizing $F(y^k, \cdot)$. The Gâteaux derivative of the data term in direction $\boldsymbol{\phi} = (\phi_1, \dots, \phi_{N_{\mathrm{mat}}})$ reads

$$\partial_{\boldsymbol{w}} \left(\int_\Sigma \int_{E_{\min}}^{E_{\max}} d_{\mathrm{KL}}(y^k, \mathfrak{I}(\boldsymbol{w}))\, \mathrm{d}\mathcal{L}^1\, \mathrm{d}\mathcal{H}^n \right)(\boldsymbol{\phi}) = \sum_{i=1}^{N_{\mathrm{mat}}} \int_\Sigma \int_{E_{\min}}^{E_{\max}} (y^k - \mathfrak{I}(\boldsymbol{w})) g_i \, \mathrm{d}\mathcal{L}^1\, \mathcal{D}\phi_i \, \mathrm{d}\mathcal{H}^n,$$

thus the optimality conditions can be computed as

$$0 \in \mathcal{D}^* \left(\int_{E_{\min}}^{E_{\max}} (y^k - \mathfrak{I}(\boldsymbol{w})) g_i \, \mathrm{d}\mathcal{L}^1 \right) + \alpha \partial R_1(\boldsymbol{w})_i - \beta(w_i - 1/N_{\mathrm{mat}}), \quad i = 1, \dots, N_{\mathrm{mat}}, \tag{3.2}$$

with $\partial R_1(\boldsymbol{w})_i$ denoting the ith component of the convex subdifferential of R_1. Multiplying pointwise by $(w_i + \varepsilon)/\mathcal{D}^*(\int_{E_{\min}}^{E_{\max}} y^k g_i \, \mathrm{d}\mathcal{L}^1)$ for some $\varepsilon > 0$ yields

$$0 \in w_i - w^{\varepsilon}_{i,y^k}(\boldsymbol{w}) + (w_i + \varepsilon) \frac{\alpha \partial R_1(\boldsymbol{w})_i - \beta(w_i - 1/N_{\mathrm{mat}})}{\mathcal{D}^*\left(\int_{E_{\min}}^{E_{\max}} y^k g_i \, \mathrm{d}\mathcal{L}^1 \right)}, \quad i = 1, \dots, N_{\mathrm{mat}},$$

where we abbreviated the forward step for the data term (which was proposed in [25] in analogy to expectation maximization for emission tomography) as

$$w^{\varepsilon}_{i,y^k}(\boldsymbol{w}) = (w_i + \varepsilon) \frac{\mathcal{D}^*\left(\int_{E_{\min}}^{E_{\max}} \mathfrak{I}(\boldsymbol{w}) g_i \, \mathrm{d}\mathcal{L}^1 \right)}{\mathcal{D}^*\left(\int_{E_{\min}}^{E_{\max}} y^k g_i \, \mathrm{d}\mathcal{L}^1 \right)} - \varepsilon. \tag{3.3}$$

We here have an ε of order 1 in mind. Taking a positive ε is crucial since we actually aim for (and encourage by our model) characteristic functions w_i. For zero ε, multiplying with $w_i + \varepsilon$ would thus lead to large parts of the optimality conditions being annihilated, and in the subsequently described algorithm this would lead to zero function values staying zero. We next view the optimality conditions as a fixed point equation for $\boldsymbol{w}$ and turn

it into a fixed point iteration by evaluating some occurrences of $\boldsymbol{w}$ at the old and some at the new iteration: To this end we introduce a damping parameter $\zeta_k \in (0,1)$ (a judicious choice of which will ensure a monotone energy decrease) and let $\boldsymbol{w}^k$ solve

$$0 \in \frac{w_i^k - (1-\zeta_k) w_i^{k-1}}{\zeta_k} - w_{i,y^k}^{\varepsilon}(\boldsymbol{w}^{k-1}) + (w_i^{k-1}+\varepsilon) \frac{\alpha \partial R_1(\boldsymbol{w}^k)_i - \beta(w_i^{k-1} - 1/N_{\mathrm{mat}})}{\mathcal{D}^*\Big(\int_{E_{\min}}^{E_{\max}} y^k g_i \,\mathrm{d}\mathcal{L}^1\Big)} \tag{3.4}$$

for $i = 1, \ldots, N_{\mathrm{mat}}$. This, however, is nothing else but the first order optimality condition of the convex minimization problem

$$\begin{aligned} \boldsymbol{w}^k &= \operatorname*{argmin}_{\boldsymbol{w}} \frac{1}{2} \int_\Omega \sum_{i=1}^{N_{\mathrm{mat}}} r_i^k \big(w_i - v_i^k\big)^2 \,\mathrm{d}\mathcal{L}^n + R_1(\boldsymbol{w}) \text{ with} \\ r_i^k &= \frac{\mathcal{D}^*\Big(\int_{E_{\min}}^{E_{\max}} y^k g_i \,\mathrm{d}\mathcal{L}^1\Big)}{\zeta_k \alpha (w_i^{k-1} + \varepsilon)} \text{ and} \\ v_i^k &= (1-\zeta_k) w_i^{k-1} + \zeta_k \left(w_{i,y^k}^{\varepsilon}(\boldsymbol{w}^{k-1}) + \frac{\beta(w_i^{k-1}+\varepsilon)(w_i^{k-1} - 1/N_{\mathrm{mat}})}{\mathcal{D}^*\Big(\int_{E_{\min}}^{E_{\max}} y^k g_i \,\mathrm{d}\mathcal{L}^1\Big)} \right). \end{aligned} \tag{3.5}$$

It turns out that ζ_k may typically be chosen at the order of 0.1, and the proposed algorithm works efficiently in case of noisy data with high regularization. However, in case of high signal-to-noise ratio (which typically means large y^k) and consequently small α, the weights r_i^k become so big that the change of $\boldsymbol{w}$ in each step of the iteration becomes neglegibly small. In this setting the algorithm requires an infeasibly large number of iterations so that we will propose an alternative algorithm for that situation.

3.2. Approximating the Lambert-W function

The computation of (3.1) requires the numerical evaluation of an expression of the form $W_0(a \exp b)/a$ for W_0 the Lambert-W function. We simply achieve this *via* Newton's method as follows. The relation $z = W_0(a \exp b)/a$ is by definition of the Lambert-W function equivalent to $az \exp(az) = a \exp b$, which can be rewritten as

$$0 = f(z) \quad \text{for} \quad f(z) = \tfrac{\log z}{a} + z - \tfrac{b}{a}.$$

The Newton iteration with iterates z^j to find the zero of f thus reads

$$z^{j+1} = z^j - \tfrac{f(z^j)}{f'(z^j)} = z^j - \tfrac{(\log z^j)/a + z^j - b/a}{1 + 1/(az^j)} = \tfrac{1 - \log z^j + b}{a + 1/z^j}.$$

We simply perform a small fixed number of iterations, starting from the initialization

$$z^0 = \begin{cases} \exp b & \text{if } a \exp b < \mathrm{e}, \\ \log a + b - \log(\log a + b)\Big(1 - \frac{1}{2\log a + 2b}\Big) & \text{else,} \end{cases}$$

which was chosen due to $W_0(s) \approx s$ for small s and $W_0(s) \approx \log(s) - \log(\log s)(1 - \frac{1}{2\log s})$ for large s.

3.3. Primal-dual iteration for weighted ROF model

Optimization problem (3.5) is a version of the well-known Rudin–Osher–Fatemi (ROF) model [41]. The difference lies in the weighted L^2-norm and the additional probability simplex constraint. Various standard convex optimization algorithms can be applied to this problem, for instance the (alternating) split Bregman iteration [17] or the equivalent alternating direction method of multipliers (ADMM) (for the equivalence see for

instance [47]). In our experiments the primal-dual iteration by Chambolle and Pock [7] converged a little faster for (3.5), which is why we briefly summarize it here.

The saddle-point formulation of (3.5) requires a dual variable $\boldsymbol{p} = (p_1, \dots, p_{N_{\text{mat}}})$ and reads

$$\min_{\boldsymbol{w}} \max_{\boldsymbol{p}} G_1(\boldsymbol{w}) - G_2(\boldsymbol{p}) + \sum_{i=1}^{N_{\text{mat}}} \langle \nabla w_i, p_i \rangle \quad \text{with}$$

$$G_1(\boldsymbol{w}) = \frac{1}{2} \int_\Omega \sum_{i=1}^{N_{\text{mat}}} r_i^k \big(w_i - v_i^k\big)^2 \,\mathrm{d}\mathcal{L}^n + \int_\Omega \iota_\Delta(\boldsymbol{w}) \,\mathrm{d}\mathcal{L}^n,$$

$$G_2(\boldsymbol{p}) = \int_\Omega \sum_{i=1}^{N_{\text{mat}}} \iota_{B_1}(p_i) \,\mathrm{d}\mathcal{L}^n,$$

where as before ι_A denotes the convex indicator function of a set A and where $B_1 \subset \mathbb{R}^n$ is the Euclidean unit ball. The corresponding primal-dual method with primal and dual step sizes $\tau, \sigma > 0$ and relaxation parameter $\theta \in [0, 1]$ then reads

$$\begin{aligned} \boldsymbol{p}^{k+1} &= \mathbf{prox}_{\sigma G_2}(\boldsymbol{p}^k + \sigma \nabla \overline{\boldsymbol{w}}^k), \\ \boldsymbol{w}^{k+1} &= \mathbf{prox}_{\tau G_1}(\boldsymbol{w}^k + \tau \operatorname{div} \boldsymbol{p}^{k+1}), \\ \overline{\boldsymbol{w}}^{k+1} &= \boldsymbol{w}^k + \theta(\boldsymbol{w}^{k+1} - \boldsymbol{w}^k) \end{aligned}$$

with $\operatorname{div} = -\nabla^*$. Abbreviating $\tilde{p}_i^k = p_i^k + \sigma \nabla \overline{w}_i^k$, the first step just becomes the pointwise projection

$$p_i^{k+1}(x) = \tilde{p}_i^k(x) / \max\{1, |\tilde{p}_i^k(x)|\} \qquad \text{for } i = 1, \dots, N_{\text{mat}}.$$

Similarly, abbreviating $\tilde{w}_i^k = w_i^k + \tau \operatorname{div} p_i^{k+1}$, the second step can be written as

$$\begin{aligned} \boldsymbol{w}^{k+1}(x) &= \operatorname*{argmin}_{\boldsymbol{w}} \frac{1}{2} \sum_{i=1}^{N_{\text{mat}}} |w_i - \tilde{w}_i^k(x)|^2 + \tau \left(\frac{1}{2} \sum_{i=1}^{N_{\text{mat}}} r_i^k(x) \big(w_i - v_i^k(x)\big)^2 \right) + \tau \iota_\Delta(\boldsymbol{w}) \\ &= \operatorname*{argmin}_{\boldsymbol{w}} \frac{1}{2} \sum_{i=1}^{N_{\text{mat}}} \left| \sqrt{1 + \tau r_i^k(x)} w_i - \frac{\tilde{w}_i^k(x) + \tau r_i^k(x) v_i^k(x)}{\sqrt{1 + \tau r_i^k(x)}} \right|^2 + \iota_\Delta(\boldsymbol{w}), \end{aligned}$$

whose solution is given by $w_i = u_i / \sqrt{1 + \tau r_i^k(x)}$ with $\boldsymbol{u} = (u_1, \dots, u_{N_{\text{mat}}})$ the orthogonal projection of $\boldsymbol{U} = ((\tilde{w}_i^k(x) + \tau r_i^k(x) v_i^k(x)) / \sqrt{1 + \tau r_i^k(x)})_{i=1,\dots,N_{\text{mat}}}$ onto the weighted simplex

$$\hat{\Delta} = \left\{ \boldsymbol{u} \in \mathbb{R}^{N_{\text{mat}}} \,\middle|\, u_1, \dots, u_{N_{\text{mat}}} \geq 0, \ \sum_{i=1}^{N_{\text{mat}}} \sqrt{1 + \tau r_i^k(x)}\, u_i = 1 \right\}.$$

Efficient (non-iterative) algorithms for projecting onto $\hat{\Delta}$ can be found *e.g.* in [39] (see [8] for fast algorithms in the unweighted case), in particular our implementation uses Algorithm 2 in [39].

3.4. Reinitialization

Being a nonconvex optimization problem (in particular due to the regularization R_2 which promotes pure materials), one cannot avoid running into local minima in which a pure material at a point x is replaced with a convex combination of other materials. To turn such a solution into one of pure materials we employ the following simple procedure. At each point $x \in \Omega$ we calculate the effective attenuation coefficient

$$g_x = \sum_{i=1}^{N_{\text{mat}}} w_i(x) g_i : [E_{\min}, E_{\max}] \to [0, \infty)$$

and identify that material j whose attenuation coefficient g_i is closest to g_x in an L^2-sense, $j = \operatorname{argmin}_i \|g_x - g_i\|_{L^2}$. We then simply reinitialize $w_j(x) = 1$ and $w_i(x) = 0$ for $i \neq j$, while all other variables stay unchanged. In practice we reinitialize repeatedly after a fixed number K of iterations, *i.e.* as reinitialization condition we use $k \bmod K = 0$.

3.5. Convergence analysis

In the following, we abbreviate by $\{a_k\}$ the sequence a_k for $k \in \mathbb{N}$. Before proving convergence of the algorithm, we show its monotonicity and provide an estimate for a feasible damping parameter.

Proposition 3.1 (Monotone descent of F)**.** *Let $\{y^k, \boldsymbol{w}^k\}$ be the sequence produced by Algorithm 1 for $\varepsilon > 0$ and damping parameters $\{\zeta_k\}$, and abbreviate*

$$G = \int_{E_{\min}}^{E_{\max}} I_0 \boldsymbol{g} \otimes \boldsymbol{g} \, \mathrm{d}\mathcal{L}^1 \in \mathbb{R}^{N_{\mathrm{mat}} \times N_{\mathrm{mat}}},$$

$$A_k^\epsilon = \int_\Omega \sum_{i=1}^{N_{\mathrm{mat}}} \frac{\mathcal{D}^*\left(\int_{E_{\min}}^{E_{\max}} y^k g_i \mathrm{d}\mathcal{L}^1\right)(w_i^k - w_i^{k-1})^2}{w_i^{k-1} + \varepsilon} \, \mathrm{d}\mathcal{L}^n \in \mathbb{R},$$

$$C_k = \frac{1}{2} \int_\Sigma (\mathcal{D}(\boldsymbol{w}^k - \boldsymbol{w}^{k-1}))^T G \mathcal{D}(\boldsymbol{w}^k - \boldsymbol{w}^{k-1}) \, \mathrm{d}\mathcal{H}^n \in \mathbb{R}$$

for $\boldsymbol{g} \otimes \boldsymbol{g}$ the outer product of the (energy-dependent) attenuation coefficient vector $\boldsymbol{g} = (g_1, \ldots, g_{N_{\mathrm{mat}}})$ with itself. Further, let $\eta \in (0, 1)$ be arbitrary. If in each iteration k we have

$$\zeta_k \leq \frac{A_k^\varepsilon}{C_k}(1 - \eta),$$

then $F(y^k, \boldsymbol{w}^k)$ is monotonically decreasing in k with

$$F(y^k, \boldsymbol{w}^k) + \frac{\eta}{\zeta_k} A_k^\varepsilon \leq F(y^k, \boldsymbol{w}^{k-1}) \leq F(y^{k-1}, \boldsymbol{w}^{k-1}).$$

Before proving the result, let us state a few properties of the involved quantities.

Lemma 3.2 (Positivity of G)**.** *If the attenuation coefficients $g_i : [E_{\min}, E_{\max}] \to [0, \infty)$ are linearly independent (as Lebesgue functions) and I_0 is positive, the matrix G from Proposition 3.1 is positive definite.*

Proof. By definition the integrand of G is positive semi-definite. Now assume $0 = \boldsymbol{w}^T G \boldsymbol{w} = \int_{E_{\min}}^{E_{\max}} I_0(E)(\boldsymbol{w}^T \boldsymbol{g}(E))^2 \, \mathrm{d}\mathcal{L}^1(E)$ for some $\boldsymbol{w} \in \mathbb{R}^{N_{\mathrm{mat}}}$, then due to the non-negativity of the integrand this implies $\sum_{i=1}^{N_{\mathrm{mat}}} w_i g_i(E) = 0$ for almost every E, contradicting the linear independence. □

Linear independence of the g_i in essence means that the materials could be reconstructed if the X-ray attenuation were measured separately for all photon energies. The resulting positive definiteness of G then implies that $C_k > 0$ unless the method has converged, *i.e.* $\boldsymbol{w}^{k-1} = \boldsymbol{w}^k$; thus the expression $\frac{A_k^\varepsilon}{C_k}$ makes sense.

Lemma 3.3 (Positivity of y^k)**.** *If the attenuation coefficients g_i are uniformly bounded and I_0 positive, then y^k is strictly positive. If in addition the measurement f is bounded below and I_0 is bounded away from zero, then also y^k is bounded away from zero with $y^k \geq \underline{y} = \mathcal{I}(\mathbf{1}) \exp(\frac{f}{\sigma^2} - W_0(\mathcal{F}(\mathbf{0}) e^{f/\sigma^2}))$ for $\mathbf{1}$ and $\mathbf{0}$ the functions with all components 1 and 0, respectively.*

Proof. This is a straightforward consequence of the definition of y^k *via* (3.1) and the positivity of $\mathcal{I}(\boldsymbol{w}^{k-1})$ as well as $\mathcal{F}(\boldsymbol{w}^{k-1})$. The explicit bound follows from the observation $\mathcal{I}(\boldsymbol{w}^{k-1}) \geq \mathcal{I}(\mathbf{1})$ and $\mathcal{F}(\boldsymbol{w}^{k-1}) \leq \mathcal{F}(\mathbf{0})$ as well as the monotonicity of W_0. □

If y^k is strictly positive, then so is A_k^ε (again unless the method has already converged) so that a feasible choice of the damping parameter ζ_k exists.

Lemma 3.4 (Lower bound on damping). *On $L^2(\Omega;\mathbb{R}^{N_{\mathrm{mat}}})$ and for positive $y^k \in L^\infty((E_{\min},E_{\max})\times\Sigma)$ consider the symmetric quadratic form*

$$Q_{y^k}(\boldsymbol{\psi},\boldsymbol{\psi}) = \frac{1}{2}\int_\Sigma \big(\mathcal{D}\big(\psi_i/s_i^k\big)\big)^T G\mathcal{D}\big(\psi_i/s_i^k\big)\,\mathrm{d}\mathcal{H}^n \quad \text{with} \quad s_i^k = \sqrt{\mathcal{D}^*\left(\int_{E_{\min}}^{E_{\max}} y^k g_i \mathrm{d}\mathcal{L}^1\right)},$$

then $\frac{A_k^\varepsilon}{C_k} \geq \frac{1}{1+\varepsilon}\frac{1}{\lambda_{y^k}}$ for $\lambda_{y^k} = \sup_{\|\boldsymbol{\psi}\|_{L^2}\leq 1} Q_{y^k}(\boldsymbol{\psi},\boldsymbol{\psi})$ the norm or maximum eigenvalue of the operator associated with Q_{y^k}.

Proof. Abbreviating $\psi_i = s_i^k(w_i^k - w_i^{k-1})$ we have

$$\frac{A_k^\varepsilon}{C_k} \geq \frac{\int_\Omega \sum_{i=1}^{N_{\mathrm{mat}}} \frac{\mathcal{D}^*\left(\int_{E_{\min}}^{E_{\max}} y^k g_i \mathrm{d}\mathcal{L}^1\right)(w_i^k - w_i^{k-1})^2}{1+\varepsilon}\,\mathrm{d}\mathcal{L}^n}{\frac{1}{2}\int_\Sigma (\mathcal{D}(\boldsymbol{w}^k - \boldsymbol{w}^{k-1}))^T G\mathcal{D}(\boldsymbol{w}^k - \boldsymbol{w}^{k-1})\,\mathrm{d}\mathcal{H}^n} = \frac{1}{1+\varepsilon}\frac{\|\boldsymbol{\psi}\|_{L^2}^2}{Q_{y^k}(\boldsymbol{\psi},\boldsymbol{\psi})}.$$

□

Remark 3.5 (Choice of damping parameter). By Lemmas 3.3 and 3.4 the damping parameter ζ_k can be chosen strictly positive. Moreover, replacing y^k in Lemma 3.4 with its lower bound $\underline{y}$ from Lemma 3.3, we obtain a feasible $\zeta_k = \frac{1}{1+\varepsilon}\frac{1-\eta}{\lambda_{\underline{y}}} > 0$ which can be computed beforehand. In our numerical computations we employed this feasible choice, and its value was typically around 0.1.

Finally, before we prove Proposition 3.1 let us rewrite the optimality condition (3.4). By inserting the definition of $w_{i,y^k}^\varepsilon(\boldsymbol{w}^{k-1})$ and multiplying with $\mathcal{D}^*(\int_{E_{\min}}^{E_{\max}} y^k g_i\,\mathrm{d}\mathcal{L}^1)/(w_i^{k-1}+\varepsilon)$ it turns into

$$\begin{aligned} 0 = {} & \frac{\mathcal{D}^*\left(\int_{E_{\min}}^{E_{\max}} y^k g_i\,\mathrm{d}\mathcal{L}^1\right)(w_i^k - w_i^{k-1})}{\zeta_k(w_i^{k-1}+\varepsilon)} \\ & - \mathcal{D}^*\left(\int_{E_{\min}}^{E_{\max}} \mathcal{I}(\boldsymbol{w}^{k-1})g_i - y^k g_i\,\mathrm{d}\mathcal{L}^1\right) + \alpha p_i^k + \beta R_2'(\boldsymbol{w}^{k-1})_i \end{aligned} \tag{3.6}$$

for $i = 1,\dots,N_{\mathrm{mat}}$, where R_2' denotes the Fréchet derivative of R_2 and $(p_1^k,\dots,p_{N_{\mathrm{mat}}}^k)$ the element of the subdifferential $\partial R_1(\boldsymbol{w}^k)$ such that the optimality condition is satisfied.

Proof of Proposition 3.1. By definition of $y^k = \operatorname{argmin} F(\cdot,\boldsymbol{w}^{k-1})$ we have $F(y^k,\boldsymbol{w}^{k-1}) \leq F(y^{k-1},\boldsymbol{w}^{k-1})$, so it remains to prove $F(y^k,\boldsymbol{w}^k) \leq F(y^k,\boldsymbol{w}^{k-1})$. Multiplying (3.6) with $w_i^k - w_i^{k-1}$, summing over i and integrating we obtain

$$\begin{aligned} 0 = {} & \frac{A_k^\varepsilon}{\zeta_k} - \int_\Omega \sum_{i=1}^{N_{\mathrm{mat}}} \mathcal{D}^*\left(\int_{E_{\min}}^{E_{\max}} \mathcal{I}(\boldsymbol{w}^{k-1})g_i - y^k g_i\,\mathrm{d}\mathcal{L}^1\right)(w_i^k - w_i^{k-1})\,\mathrm{d}\mathcal{L}^n \\ & + \alpha \sum_{i=1}^{N_{\mathrm{mat}}} \big\langle\, p_i^k, w_i^k - w_i^{k-1}\big\rangle + \beta\big\langle R_2'(\boldsymbol{w}^{k-1}), \boldsymbol{w}^k - \boldsymbol{w}^{k-1}\big\rangle. \end{aligned}$$

By definition of the subgradient and by the convexity of $-R_2$ we have

$$\sum_{i=1}^{N_{\mathrm{mat}}} \big\langle p_i^k, w_i^k - w_i^{k-1}\big\rangle \geq R_1(\boldsymbol{w}^k) - R_1(\boldsymbol{w}^{k-1}),$$

$$\left\langle R_2'(\boldsymbol{w}^{k-1})_i, \boldsymbol{w}^k - \boldsymbol{w}^{k-1} \right\rangle \geq R_2(\boldsymbol{w}^k) - R_2(\boldsymbol{w}^{k-1}),$$

so that the previous equality can be turned into the inequality

$$\begin{aligned}
&\alpha R_1(\boldsymbol{w}^k) + \beta R_2(\boldsymbol{w}^k) - \alpha R_1(\boldsymbol{w}^{k-1}) - \beta R_2(\boldsymbol{w}^{k-1}) + \frac{A_k^\varepsilon}{\zeta_k} \\
&\qquad \leq \int_\Sigma \sum_{i=1}^{N_{\text{mat}}} \left(\int_{E_{\min}}^{E_{\max}} \mathfrak{I}(\boldsymbol{w}^{k-1}) g_i - y^k g_i \, \mathrm{d}\mathcal{L}^1 \right) \mathcal{D}(w_i^k - w_i^{k-1}) \, \mathrm{d}\mathcal{H}^n.
\end{aligned}$$

Abbreviating the Kullback–Leibler fidelity term as

$$L(\boldsymbol{w}) = \int_\Sigma \int_{E_{\min}}^{E_{\max}} d_{KL}(y^k, \mathfrak{I}(\boldsymbol{w})) \, \mathrm{d}\mathcal{L}^1 \, \mathrm{d}\mathcal{H}^n,$$

we now add the difference $L(\boldsymbol{w}^k) - L(\boldsymbol{w}^{k-1})$ on both sides in order to achieve a term $F(y^k, \boldsymbol{w}^k) - F(y^k, \boldsymbol{w}^{k-1})$,

$$\begin{aligned}
&F(y^k, \boldsymbol{w}^k) - F(y^k, \boldsymbol{w}^{k-1}) + \frac{A_k^\varepsilon}{\zeta_k} \\
&\leq - \sum_{i=1}^{N_{\text{mat}}} \int_\Sigma \left[\int_{E_{\min}}^{E_{\max}} y^k g_i - \mathfrak{I}(\boldsymbol{w}^{k-1}) g_i \, \mathrm{d}\mathcal{L}^1 \right] \mathcal{D}(w_i^k - w_i^{k-1}) \, \mathrm{d}\mathcal{H}^n + L(\boldsymbol{w}^k) - L(\boldsymbol{w}^{k-1}) \\
&= L(\boldsymbol{w}^k) - L(\boldsymbol{w}^{k-1}) - \langle L'(\boldsymbol{w}^{k-1}), \boldsymbol{w}^k - \boldsymbol{w}^{k-1} \rangle,
\end{aligned}$$

where L' denotes the Fréchet derivative of L. Using Taylor's theorem, the right-hand side of the inequality can be expressed as a second directional derivative of L,

$$\begin{aligned}
L(\boldsymbol{w}^k) - L(\boldsymbol{w}^{k-1}) - \langle L'(\boldsymbol{w}^{k-1}), \boldsymbol{w}^k - \boldsymbol{w}^{k-1} \rangle &= \frac{1}{2} \frac{\mathrm{d}^2}{\mathrm{d}t^2} L(\boldsymbol{w}^{k-1} + t(\boldsymbol{w}^k - \boldsymbol{w}^{k-1}))|_{t=\tau} \\
&= \frac{1}{2} \int_\Sigma \sum_{i,k=1}^{N_{\text{mat}}} \int_{E_{\min}}^{E_{\max}} I_0 \exp(-\boldsymbol{g} \cdot \mathcal{D}\boldsymbol{z}) \mathcal{D}\phi_i g_i \mathcal{D}\phi_k g_k \, \mathrm{d}\mathcal{L}^1 \, \mathrm{d}\mathcal{H}^n \\
&\leq \frac{1}{2} \int_\Sigma (\mathcal{D}\boldsymbol{\phi})^T G \mathcal{D}\boldsymbol{\phi} \, \mathrm{d}\mathcal{H}^n,
\end{aligned}$$

where we abbreviated $\boldsymbol{\phi} = (\boldsymbol{w}^k - \boldsymbol{w}^{k-1})$ and $\boldsymbol{z} = \boldsymbol{w}^{k-1} + \tau(\boldsymbol{w}^k - \boldsymbol{w}^{k-1})$ for some $\tau \in [0, 1]$. Summarizing, we arrive at

$$F(y^k, \boldsymbol{w}^k) - F(y^k, \boldsymbol{w}^{k-1}) + \frac{A_k^\varepsilon}{\zeta_k} \leq C_k$$

or equivalently

$$F(y^k, \boldsymbol{w}^k) + \frac{\eta}{\zeta_k} A_k^\varepsilon + \frac{1-\eta}{\zeta_k} A_k^\varepsilon \leq C_k + F(y^k, \boldsymbol{w}^{k-1}),$$

which implies $F(y^k, \boldsymbol{w}^k) + \frac{\eta}{\zeta_k} A_k^\varepsilon \leq F(y^k, \boldsymbol{w}^{k-1})$ if $\frac{1-\eta}{\zeta_k} A_k^\varepsilon \geq C_k$. □

Next we prove convergence of Algorithm 1 to a critical point of the functional F. We follow essentially the same steps as in [5,37,44].

Theorem 3.6 (Convergence of damped alternating minimization)**.** *Assume I_0 to be integrable and $\boldsymbol{g}$ and f to be bounded. Also assume I_0 and $\boldsymbol{g}$ to be bounded away from zero. Let $\{y^k, \boldsymbol{w}^k\}$ be the sequence produced by Algorithm 1 for $\varepsilon > 0$ and damping parameters $\{\zeta_k\}$ satisfying the condition from Proposition 3.1 and being uniformly bounded and bounded away from zero (which is possible by Rem. 3.5). Then every subsequence of $\{y^k, \boldsymbol{w}^k\}$ contains a subsequence converging strongly in $L^1((E_{\min}, E_{\max}) \times \Sigma) \times L^q(\Omega)^{N_{\text{mat}}}$ for any $q \in [1, \infty)$, and every limit point of the sequence is a critical point of F.*

Proof. We proceed in three steps.

(1) From coercivity of F and Proposition 3.1 we derive convergence of $\boldsymbol{w}^k$ and y^k along a subsequence.
(2) We exploit the optimality condition to derive convergence of the dual variables p_i^k.
(3) We show that the limit satisfies the optimality conditions for a critical point of F.

Step 1 – convergence of the primal iterates. Proposition 3.1 implies

$$\alpha \sum_{i=1}^{N_{\mathrm{mat}}} \mathrm{TV}(w_i^k) - \frac{\beta}{2}\mathcal{L}^n(\Omega)(1-1/N_{\mathrm{mat}})^2 \le F(y^k, \boldsymbol{w}^k) \le F(y^0, \boldsymbol{w}^0) < \infty$$

so that $\boldsymbol{w}^k$ is uniformly bounded in $[L^\infty(\Omega)\cap \mathrm{BV}(\Omega)]^{N_{\mathrm{mat}}}$. Thus, any subsequence of $\{\boldsymbol{w}^k\}$ contains another subsequence $\{\boldsymbol{w}^{k_n}\}$ converging weakly-*in $[L^\infty(\Omega)\cap \mathrm{BV}(\Omega)]^{N_{\mathrm{mat}}}$ to some $\boldsymbol{w}$. By the compact embedding $\mathrm{BV}(\Omega) \hookrightarrow L^1(\Omega)$ and Hölder's inequality this implies $\boldsymbol{w}^{k_n} \to \boldsymbol{w}$ strongly in $L^q(\Omega)^{N_{\mathrm{mat}}}$ as $n \to \infty$ for any $q \in [1,\infty)$. In fact, we even have $\boldsymbol{w}^{k_n+K} \to \boldsymbol{w}$ for any fixed integer K. Indeed, Proposition 3.1 yields

$$F(y^k, \boldsymbol{w}^k) \le F(y^{k-1}, \boldsymbol{w}^{k-1}) - \frac{\eta}{\zeta_k} A_k^\varepsilon \le \cdots \le F(y^0, \boldsymbol{w}^0) - \eta \sum_{i=1}^{k} \frac{A_i^\varepsilon}{\zeta_i}$$

so that $\sum_{i=1}^\infty A_i^\varepsilon$ is bounded and thus $A_k^\varepsilon \to 0$ as $k \to \infty$. Now Lemma 3.3 implies $\mathcal{D}^*\Big(\int_{E_{\min}}^{E_{\max}} y^k g_i \,\mathrm{d}\mathcal{L}^1\Big)/(w_i^{k-1}+\varepsilon) > c$ for some positive constant c independent of k so that, by the definition of A_k^ε,

$$c\|\boldsymbol{w}^k - \boldsymbol{w}^{k-1}\|_{L^2}^2 \le A_k^\varepsilon \to 0.$$

Again by Hölder's inequality we obtain $\|\boldsymbol{w}^k - \boldsymbol{w}^{k-1}\|_{L^q} \to 0$ as $k \to \infty$ for any $q \in [1,\infty)$ and therefore by induction $\boldsymbol{w}^{k_n+K} \to \boldsymbol{w}$ as $n \to \infty$.
Next consider the convergence of y^k. By Lemma 2.4 we have $\mathcal{F}(\boldsymbol{w}^{k_n-1}) \to \mathcal{F}(\boldsymbol{w})$ in $L^1(\Sigma)$ so that also $Y_{\boldsymbol{w}^{k_n-1}} \to Y_{\boldsymbol{w}}$ in $L^1(\Sigma)$ as $n \to \infty$ for the quantity from Lemma 2.6. Now by Lemma 2.6 we have

$$y^{k_n} = y_{\boldsymbol{w}^{k_n-1}} = \mathcal{I}(\boldsymbol{w}^{k_n-1}) \exp\Big(\tfrac{f-Y_{\boldsymbol{w}^{k_n-1}}}{\sigma^2}\Big) = I_0 \exp\Bigg(-\sum_{i=1}^{N_{\mathrm{mat}}} g_i \mathcal{D} w_i^{k_n-1} + \tfrac{f-Y_{\boldsymbol{w}^{k_n-1}}}{\sigma^2}\Bigg).$$

Repeating the argument of Lemma 2.4 (only with $-\sum_{i=1}^{N_{\mathrm{mat}}} g_i \mathcal{D} w_i$ replaced by $-\sum_{i=1}^{N_{\mathrm{mat}}} g_i \mathcal{D} w_i + \frac{f-Y_{\boldsymbol{w}}}{\sigma^2}$) we obtain

$$y^{k_n} \to y = y_{\boldsymbol{w}}$$

strongly in $L^1((E_{\min}, E_{\max})\times\Sigma)$ as $n \to \infty$. Note that from the mere coercivity of F we would only have obtained weak convergence of a subsequence of y^{k_n} to y.

Step 2 – convergence of dual iterates. We first prove that $\int_{E_{\min}}^{E_{\max}} \mathcal{I}(\boldsymbol{w}^{k_n-1}) g_i \,\mathrm{d}\mathcal{L}^1$ converges in any $L^q(\Sigma)$ with $q \in [1,\infty)$. Indeed, exploiting that the exponential function has unit Lipschitz constant on the negative real axis,

$$\begin{aligned}
&\int_\Sigma \left(\int_{E_{\min}}^{E_{\max}} \mathcal{I}(\boldsymbol{w}^{k_n-1}) g_i \,\mathrm{d}\mathcal{L}^1 - \int_{E_{\min}}^{E_{\max}} \mathcal{I}(\boldsymbol{w}) g_i \,\mathrm{d}\mathcal{L}^1 \right)^q \mathrm{d}\mathcal{H}^n \\
&\quad \le \int_\Sigma \left(\int_{E_{\min}}^{E_{\max}} I_0(E) g_i(E) \left| \exp\left(-\sum_{j=1}^{N_{\mathrm{mat}}} g_j \mathcal{D} w_j^{k_n-1} \right) - \exp\left(-\sum_{j=1}^{N_{\mathrm{mat}}} g_j \mathcal{D} w_j \right) \right| \mathrm{d}\mathcal{L}^1 \right)^q \mathrm{d}\mathcal{H}^n \\
&\quad \le \int_\Sigma \left(\int_{E_{\min}}^{E_{\max}} I_0(E) g_i(E) \sum_{j=1}^{N_{\mathrm{mat}}} g_j \left| \mathcal{D}(w_j^{k_n-1} - w_j) \right| \mathrm{d}\mathcal{L}^1 \right)^q \mathrm{d}\mathcal{H}^n
\end{aligned}$$

$$\leq \left(\int_{E_{\min}}^{E_{\max}} I_0(E) g_i(E) \max_j g_j(E) \,\mathrm{d}\mathcal{L}^1 \right)^q \int_\Sigma \left| \mathcal{D}(\boldsymbol{w}^{k_n-1} - \boldsymbol{w}) \right|^q \mathrm{d}\mathcal{H}^n,$$

which converges to zero as $\mathcal{D}(w_i^{k_n-1} - w_i) \to 0$ in $L^q(\Sigma)$ by the continuity of $\mathcal{D}$. As a consequence, for $n \to \infty$ we also have the limit

$$\int_{E_{\min}}^{E_{\max}} y^{k_n} g_i \,\mathrm{d}\mathcal{L}^1 = \int_{E_{\min}}^{E_{\max}} \mathcal{I}(\boldsymbol{w}^{k_n-1}) g_i \,\mathrm{d}\mathcal{L}^1 \exp\left(\tfrac{f - Y_{\boldsymbol{w}^{k_n-1}}}{\sigma^2}\right) \to \int_{E_{\min}}^{E_{\max}} y g_i \,\mathrm{d}\mathcal{L}^1$$

strongly in any $L^q(\Sigma)$ with $q \in [1, \infty)$ (recall that $Y_{\boldsymbol{w}^{k_n-1}}$ converges in $L^1(\Sigma)$ and thus the exponential term converges in any $L^q(\Sigma)$). Now we can rewrite (3.6) as

$$p_i^{k_n} = \frac{\mathcal{D}^*\left(\int_{E_{\min}}^{E_{\max}} y^{k_n} g_i \,\mathrm{d}\mathcal{L}^1\right)(w_i^{k_n} - w_i^{k_n-1})}{-\alpha \zeta_{k_n}(w_i^{k_n-1} + \varepsilon)} + \frac{1}{\alpha}\mathcal{D}^*\left(\int_{E_{\min}}^{E_{\max}} \mathcal{I}(\boldsymbol{w}^{k_n-1}) g_i - y^{k_n} g_i \,\mathrm{d}\mathcal{L}^1\right) + \frac{\beta}{\alpha}\left(w_i^{k_n-1} - \frac{1}{N_{\mathrm{mat}}}\right),$$

which by the continuity of $\mathcal{D}^*$ converges strongly in any $L^q(\Omega)$ with $q \in [1, \infty)$ to

$$p_i = \frac{1}{\alpha}\mathcal{D}^*\left(\int_{E_{\min}}^{E_{\max}} \mathcal{I}(\boldsymbol{w}) g_i - y g_i \,\mathrm{d}\mathcal{L}^1\right) + \frac{\beta}{\alpha}\left(w_i - \frac{1}{N_{\mathrm{mat}}}\right). \tag{3.7}$$

By the continuous embedding of $\mathrm{BV}(\Omega)$ into $L^{\frac{n}{n-1}}(\Omega)$ this also implies weak-*convergence of $p_i^{k_n}$ to p_i in the dual space $\mathrm{BV}(\Omega)^*$.

Step 3 – criticality of limit. We first show that $p_i \in \partial R_1(w_i)$. To this end let $z \in \mathrm{BV}(\Omega)$ be arbitrary, then

$$R_1(w_i^{k_n}) + \langle p_i^{k_n}, z - w_i^{k_n} \rangle \leq R_1(z)$$

since $p_i^{k_n}$ is a subgradient of R_1 at $w_i^{k_n}$. Due to the sequential lower semi-continuity of R_1 and the strong convergence of both $p_i^{k_n}$ and $w_i^{k_n}$ in any Lebesgue space, taking the limit $n \to \infty$ on both sides yields

$$R_1(w_i) + \langle p_i, z - w_i \rangle \leq R_1(z).$$

By the arbitrariness of z we see $p_i \in \partial R_1(w_i)$. Therefore, (3.7) implies that the optimality condition (3.2) for minimizing F with respect to $\boldsymbol{w}$ is satisfied. The optimality condition for minimizing F with respect to y is also satisfied due to $y = y_{\boldsymbol{w}}$, hence the point $(y, \boldsymbol{w})$ is critical for F.

□

4. Numerical results

As examples supporting the feasibility and usefulness of the proposed model we will reconstruct a phantom from measurements with different noise levels.

4.1. Phantom data

We use the phantom from [16] (Fig. 1 left) consisting of disks of different materials (we will use up to six different materials including air). The different materials also stem from [16] and are specified in Figure 1 (middle) together with their attenuation coefficients g_i, which are taken from the NIST dataset www.nist.gov/pml/data/xraycoef/. The intensity I_0 emitted by the X-ray source per space angle is taken as $I_0(E) = \bar{I} i_0(E)$

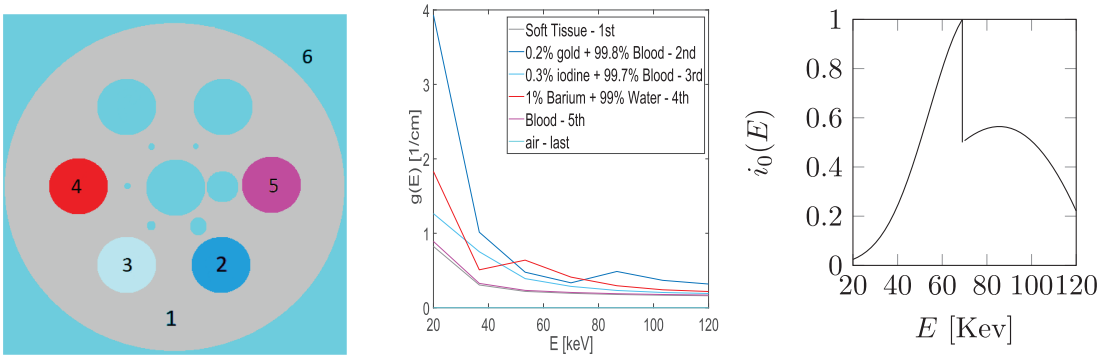

(a) (b) (c)

FIGURE 1. Employed phantom with material indicated by number (note that during the first experiments we use air instead of blood in region 5) (a), attenuation coefficients of the different materials (b), intensity profile of the X-ray source (c).

for the profile i_0 shown in Figure 1 right (taken from [42]) and $\bar{I}$ modelling the source strength and thereby the signal to noise ratio.

In our numerical experiments we actually discretize the photon energy range $[E_{\min}, E_{\max}]$ by seven discrete energy levels and the phantom by 64×64 pixels (we also tested higher resolutions, and the results did not change much).

Measurements are obtained by computing the forward operator $\mathcal{I}(w)(E, \boldsymbol{x}, \boldsymbol{\theta})$, imposing Poisson noise to obtain $y(E, \boldsymbol{x}, \boldsymbol{\theta})$, integrating this y in E and finally adding Gaussian noise of different standard deviations σ.

4.2. Reconstructions for different noise settings

We will perform reconstructions for three different noise settings:

(a) low Poisson and low Gaussian noise (high signal to noise ratio),
(b) high Poisson and low Gaussian noise (low X-ray source intensity),
(c) high Poisson and high Gaussian noise (low X-ray source intensity & detector quality).

The standard deviation for Gaussian noise in the three cases is taken as $\sigma = 2 \cdot 10^{-3}, 2 \cdot 10^{-6}, 10^2$, respectively. The X-ray source intensity in the cases is taken as $\bar{I} = 3 \cdot 10^{11}, 1500$, and again 1500. We employ sinograms with 180 evenly spaced views $\boldsymbol{\theta}$ between 0° and 180° and a resolution of 95 bins per view. Examples of the corresponding sinograms along with their histograms are shown in Figure 2.

For each noise setting (a)–(c) we run the reconstruction using our main algorithm from Section 3, but we also test the two alternatives described in the appendix in Sections A and B. In the following we abbreviate the algorithms as FBS (forward backward splitting), PD (primal-dual), and ADMM (alternating direction of multipliers method).

We used the FBS algorithm to tune optimal regularization parameters α and β for each noise scenario (a)–(c) and to assess how reconstructions are affected by different reinitialization frequencies (see Sect. 3.4). Computations were parallelized on a JupyterHub server (vCPU 2.0–16.0, 64 GB RAM). For all noise cases, initial values $(y^0, \boldsymbol{w}^0)$ were set to $0.1 \cdot (\mathbf{1}, \bar{\mathbf{1}})$, with $\mathbf{1}$ and $\bar{\mathbf{1}}$ as all-ones tensors sized $180 \times 95 \times 7$ (view angles × bins × discrete photon energies) and $64 \times 64 \times 5$ (pixels along first × second direction × number of materials). The iteration number was fixed at 23 000 and the damping parameter to $\zeta = 0.1$. Inner primal-dual iterations from Section 3.3 used step lengths $\tau = 0.02$, $\sigma = 6.25$, relaxation parameter $\theta = 0.1$, and 1000 iterations. Reconstructions are evaluated by the mean SSIM score of the different spatial material distributions $w_1, \ldots, w_{N_{\text{mat}}}$. Table 1 details the number of runs for different parameter combinations as well as the tested parameter ranges per noise case,

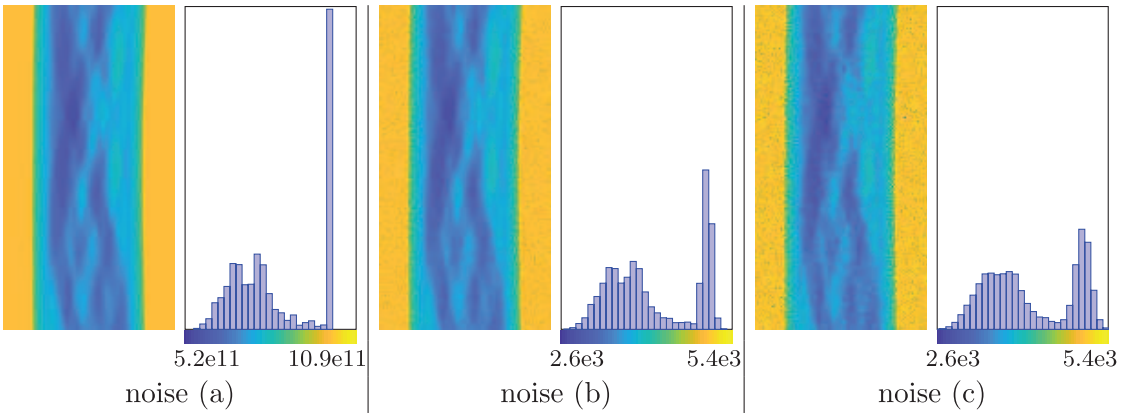

FIGURE 2. Measured sinograms for the three different noise settings along with the histograms of their values indicating the amount of spreading due to noise.

TABLE 1. Tested parameter ranges and median CPU time for the FBS algorithm in the different noise cases. The third column provides the number of iterations between two reinitializations according to Section 3.4.

Noise case	#param. settings	reinit. iterations	α	β	median CPU time (s)
(a)	420	[3e3, 11e3], none	[1e4, 7e6]	[0, 1e–1]	4.95e3
(b)	432	[3e3, 11e3], none	[1e–2, 1e1]	[0, 1e–3]	8.01e3
(c)	432	[3e3, 11e3], none	[1e–2, 1e1]	[0, 1e–3]	8.40e3

TABLE 2. Optimal parameters for the FBS algorithm.

Noise case	reinit. iterations	α	β
(a)	11e3	1e6	1e–1
(b)	11e3	7e–2	0
(c)	11e3	7e–2	0

alongside median CPU time. Figure 3 presents heat maps of the mean SSIM for different values of α and β across various reinitialization frequencies and noise cases. For noise case (a) with high-intensity X-ray source, higher α values were necessary to balance the dominant Kullback–Leibler term.

The benefit of the reinitialization procedure becomes apparent in Figure 3, where consistently higher SSIM values are achieved with than without reinitialization. The reconstruction quality is not sensitive to the reinitialization frequency, though. While in each noise case there is a (finite, but not too narrow) range of good values for α, reconstruction quality seems independent of the chosen value for β. Note that even though β seems to have little influence experimentally, we still regard it interesting for the theoretical model and convergence analysis to include the associated nonconvex term. Table 2 summarizes the optimal parameter values. We employ these values for α and β throughout the remainder of the section.

For the PD algorithm we employ 500 maximum inner primal-dual iterations with a relaxation parameter $\theta = 1$ and step sizes $\rho_1 = \frac{1}{100}$, $\rho_2 = \frac{1}{200}$, $\tau = \frac{1}{56}$. We initialize the primal variables $(y^0, \boldsymbol{w}^0)$ as in the FBS algorithm and

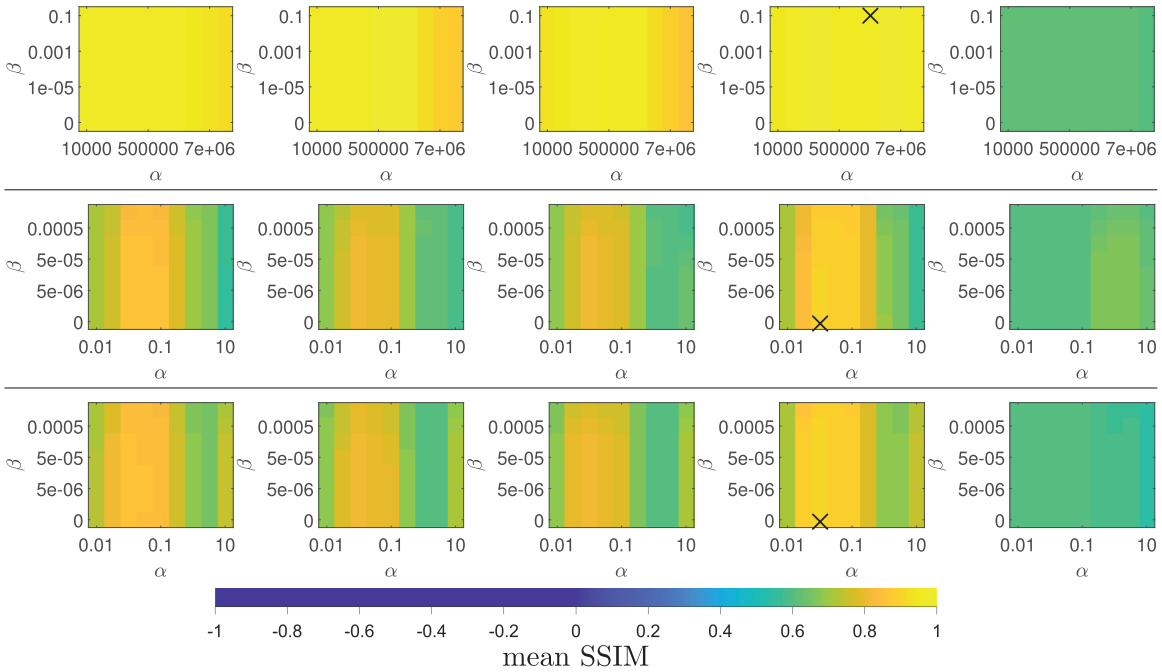

FIGURE 3. Mean SSIM heat maps for different values of α and β at various reinitialization frequencies (after 3000, 6000, 9000, 11 000 iterations and never). Rows correspond to noise levels (a)–(c). The cross in each row indicates the optimal parameter setting.

the dual variables as $(\phi^0, \psi^0) = (\mathbf{0}, \bar{\mathbf{0}})$, where $\mathbf{0}$ and $\bar{\mathbf{0}}$ are all-zeros tensors of sizes $180 \times 95 \times 5$ and $64 \times 64 \times 5 \times 2$, respectively. We further perform 55 outer iterations. As for the FBS algorithm, the optimal reconstruction for each noise scenario is identified by the best mean SSIM score. Specifically, the best reconstructions occur with reinitialization every 25, 5, and 5 iterations for the noise cases (a), (b), and (c), respectively, with corresponding median CPU times of 3.64e3, 3.11e3, and 3.14e3 seconds. As for the FBS algorithm, different reinitialization frequencies yield very similar results.

Finally, we also perform parameter tests with the ADMM algorithm. We fix the number of iterations at 500. The primal variables $(y^0, \boldsymbol{w}^0, \tilde{\boldsymbol{w}}^0)$ are initialized as (1e–2$\mathbf{1}$, 1e–1$\bar{\mathbf{1}}$, 1e–1$\bar{\mathbf{1}}$), and dual variables $(\Lambda^0, \lambda_1^0, \lambda_2^0)$ as zero tensors. As before we explore the influence of all algorithmic parameters, in particular the three Lagrange penalties μ_1, μ_2, μ_3 and the reinitialization frequency. Table 3 and Figure 4 show the range of tested parameter values and the corresponding mean SSIM heat maps.

As for the FBS algorithm the use of the reinitialization consistently leads to better reconstructions than without, while for a large range of reinitialization frequencies a similar behaviour is observed. Table 4 presents the optimal parameter values, in particular those for μ_1, μ_2, μ_3.

The actual reconstructions along with the mean SSIM values for the three noise settings are provided in Figure 5. In noise case (a) the reconstructions are very clean and almost equal the ground truth, while small features (the smaller holes) are removed in the results for noise cases (b) and (c). In addition, in these cases the different materials sometimes got mixed up, either in small subregions near the boundary between two materials or for a complete material, where in noise case (c) both PD and ADMM and in noise case (b) PD reach a local minimum interpreting ground truth material 2 as material 4.

Figure 6 illustrates how the objective function decreases with each iteration for different algorithms and noise levels, plotting $\log_{10} F(y^k, \boldsymbol{w}^k)$ for $k = 1, 2, \ldots$. The graphs also include three horizontal lines: (red) the

TABLE 3. Tested parameter ranges and median CPU time for the ADMM algorithm in the different noise cases.

Noise case	# param. settings	reinit. iterations	μ_1	μ_2	μ_3	median CPU time (s)
(a)	750	[50, 450], none	$\left[\frac{1e11}{64}, \frac{1e18}{64}\right]$	$\left[\frac{1e10}{64}, \frac{1e18}{64}\right]$	$\left[\frac{1e8}{64}, \frac{4e10}{64}\right]$	211.30
(b)	750	[50, 450], none	$\left[\frac{1e3}{64}, \frac{1e9}{64}\right]$	$\left[\frac{1e3}{64}, \frac{1e9}{64}\right]$	$\left[\frac{1e1}{64}, \frac{1e7}{64}\right]$	287.94
(c)	750	[50, 450], none	$\left[\frac{0.8e1}{64}, \frac{1e5}{64}\right]$	$\left[\frac{0.8e1}{64}, \frac{1e5}{64}\right]$	$\left[\frac{0.7e1}{64}, \frac{1e2}{64}\right]$	338.31

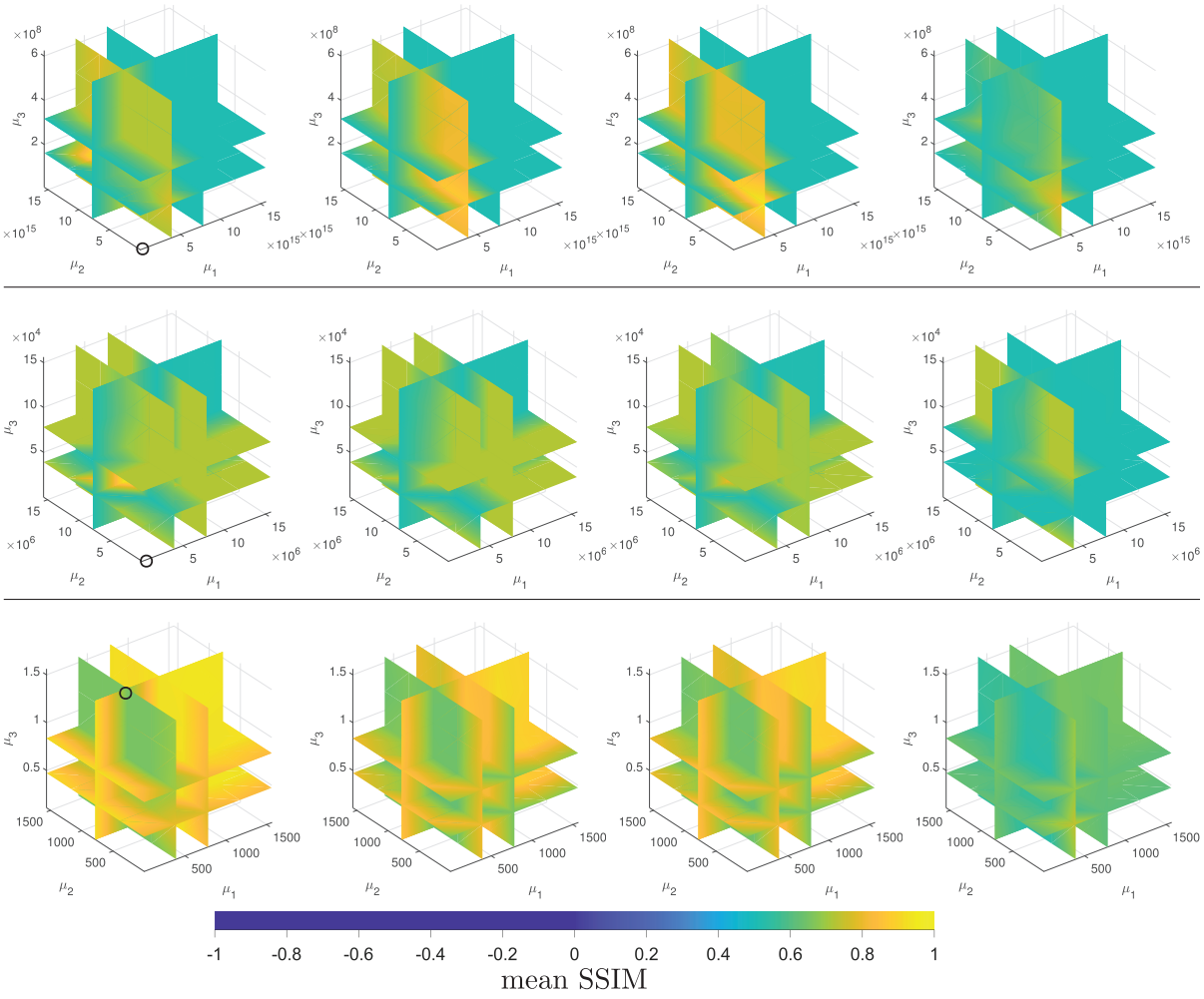

FIGURE 4. Mean SSIM heat maps for different values of μ_1, μ_2 and μ_3 at various reinitialization frequencies (after 50, 250, 450 iterations and never). Rows correspond to noise levels (a)–(c). The circle in each row indicates the optimal parameter setting.

TABLE 4. Optimal parameters for the ADMM algorithm.

Noise case	reinit. iterations	(μ_1, μ_2, μ_3)
(a)	50	(1e11, 1e10, 4e8)/64
(b)	50	(1e3, 1e3, 1e1)/64
(c)	50	(2.5e4, 2.5e4, 1e2)/64

energy $\log_{10} F(y^\star, \boldsymbol{w}^\star)$ of the sinograms $y^\star$ without Gaussian (but with Poisson) noise and the ground truth materials $\boldsymbol{w}^\star$; (yellow) the energy $\log_{10} F(y^{N_{\text{iter}}}, \boldsymbol{w}^\star)$ of the predicted sinograms at the last iteration (N_{iter}) with ground truth materials; (purple) the energy $\log_{10} F(y^\star, \boldsymbol{w}^{N_{\text{iter}}})$ of the sinograms without Gaussian noise and the final iteration's material output. For low noise (a), all three lines align, and $\log_{10} F(y^k, \boldsymbol{w}^k)$ approaches them. For moderate noise (b), FBS and ADMM energies are notably lower than $\log_{10} F(y^\star, \boldsymbol{w}^\star)$ and closer to $\log_{10} F(y^{N_{\text{iter}}}, \boldsymbol{w}^\star)$, unlike PD where energy drops further. This is reflected in Figure 5, showing FBS and ADMM reconstructions match the ground truth better than PD reconstructions, which blend materials 2 and 4. Figure 7 shows reconstructions and the mean SSIM values for noise case (a) with an additional material taken to have almost the same attenuation behaviour as soft tissue to produce a highly challenging situation with two very similar materials. All algorithms produce spurious pixels, where the effect is the strongest for the FBS algorithm – as already predicted in Section 3 it is quite slow in removing artefacts in the low noise case.

4.3. Statistical evaluation

Separating nearby materials such as blood and tissue is highly ill-posed. Sometimes it is successful as exemplified in previous examples, but oftentimes noise will prevent correct material identification, leading to a minimizer of the variational model with incorrect materials, or the optimization algorithm reaches a local minimum with incorrect material identification. Of course, further algorithmic finetuning or additional material priors for the application at hand may greatly improve this situation. However, we want to test the effectiveness of the material decomposition without additional prior knowledge. To this end we generate 700 random test phantoms of 64×64 pixels, each with 1 to 5 materials plus air, where each material occupies one or two random discs. For each phantom the random disc locations and radii are chosen consecutively according to the uniform distribution under the constraint that they are at least four pixels in diameter and have at least two pixels distance from the previous discs and the boundary. The materials and source spectrum are the same as in Figure 1, and we take the setting of high Poisson and high Gaussian noise. Reconstructions are performed with the ADMM algorithm. We use ADMM here since it proved the fastest choice in the previous simulations. (Note, however, that the FBS algorithm has fewer hyperparameters that affect reconstruction accuracy compared to ADMM with its parameters μ_1, μ_2, μ_3; recall that the only algorithmic parameter ζ is fixed by Rem. 3.5). For each subgroup of phantoms with same number of materials we chose the numerical parameters such that they visually worked well for a single example phantom and then kept these parameters for all other phantoms, see Table 5. In Table 6 we provide for each case of two to six total materials the number of random phantoms, the mean CPU time, as well as the mean SSIM between the ground truth and the reconstruction of each material. As previously, the simulations were parallelized and executed on a JupyterHub server (vCPU 2.0–16.0, 64 GB RAM).

Due to the high noise, already for just air plus another material the SSIM deviates from the optimal value 1. It decreases as the number of materials and thus the problem difficulty increases. In particular, the worst values are seen for materials 1 and 5 (soft tissue and blood), which are difficult to separate, as expected. However, the mean SSIM is still above 0.6, meaning a successful separation in most cases.

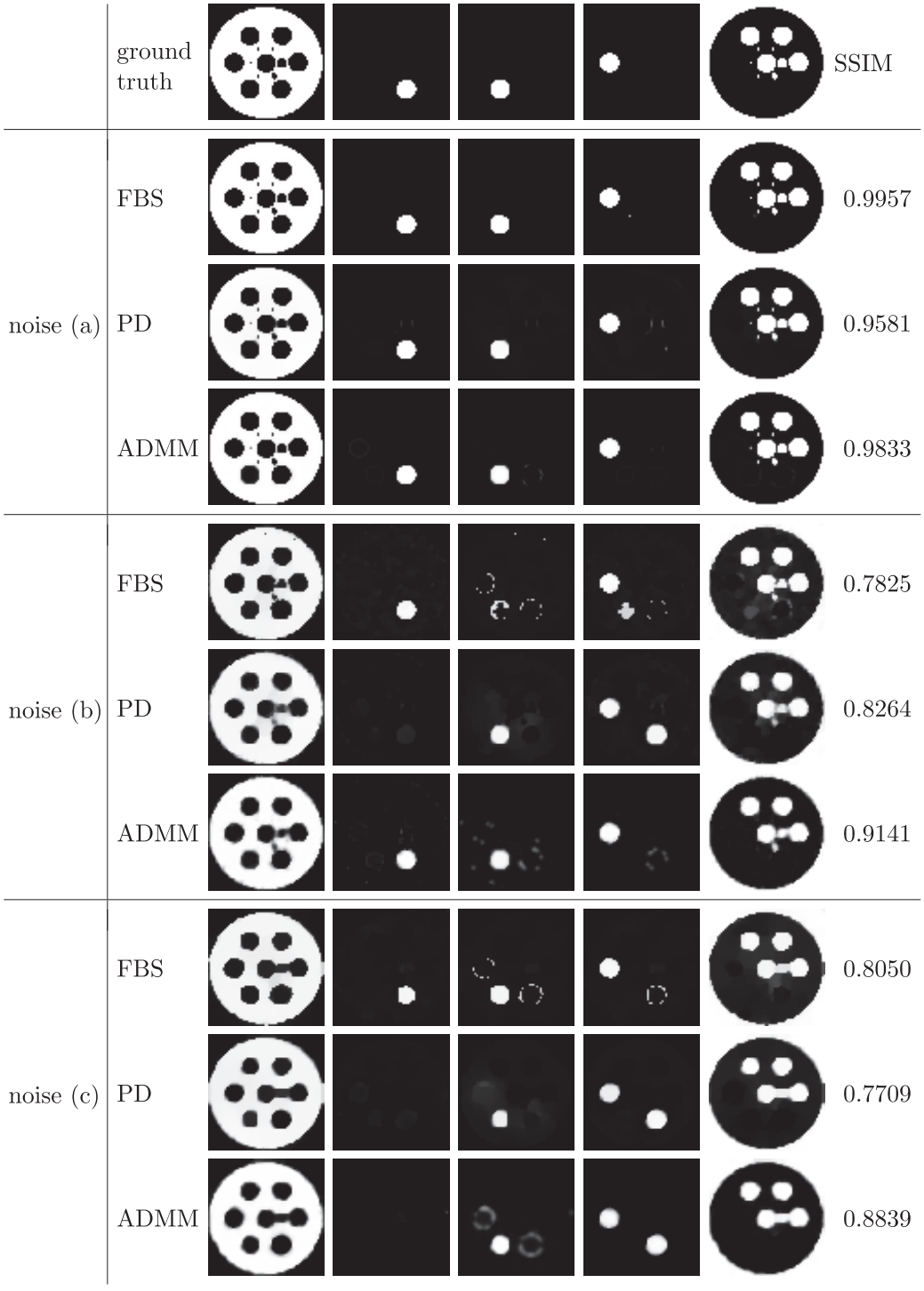

FIGURE 5. Reconstructed materials for the different noise settings and algorithms.

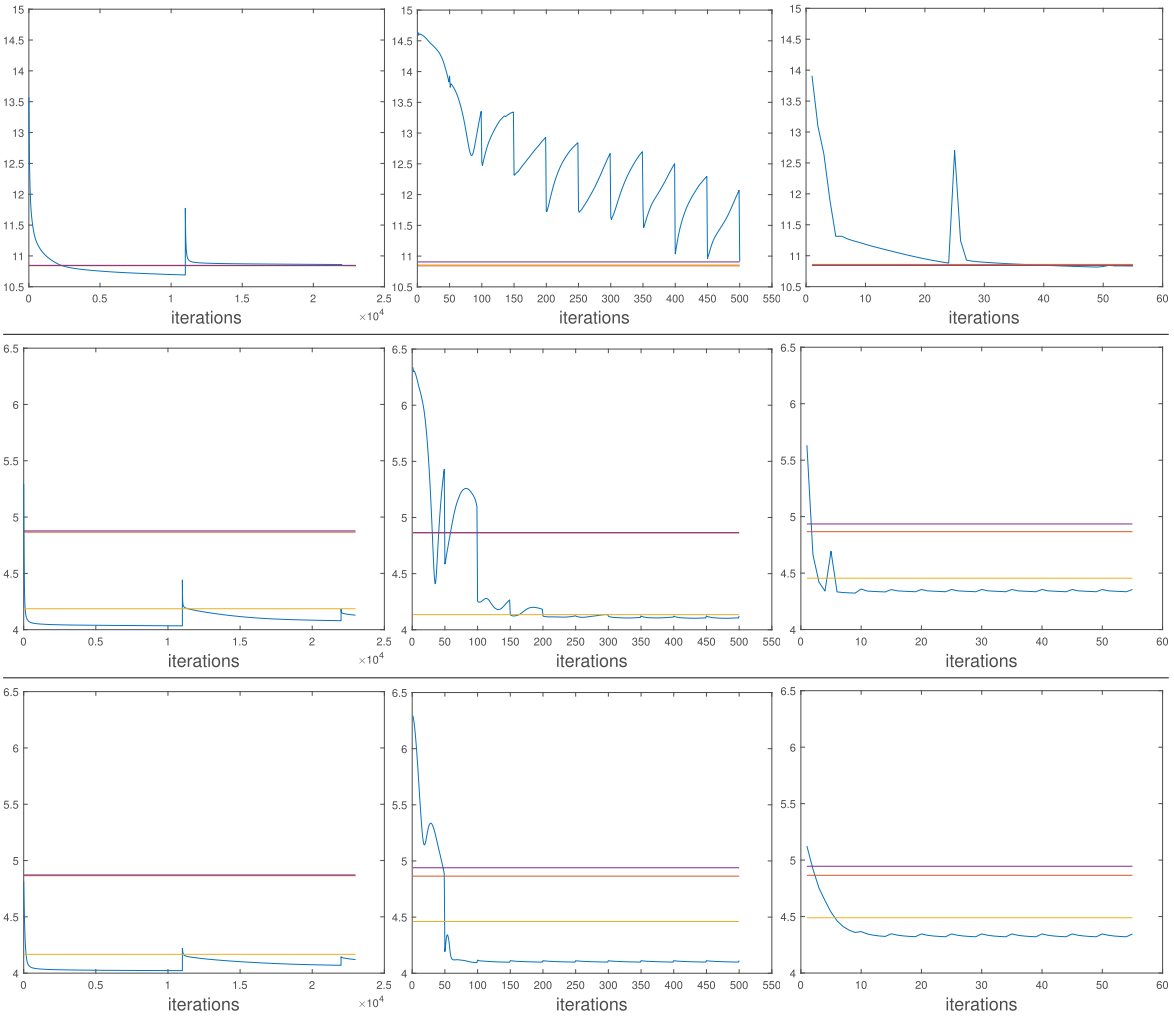

FIGURE 6. Objective function decrease (blue line) for each algorithm and noise level. Rows represent noise levels (a) to (c), and columns represent the FBS, ADMM, and PD algorithms. Spikes are caused by reinitialization. The red, yellow and purple lines indicate $\log_{10} F(y^\star, \boldsymbol{w}^\star)$, $\log_{10} F(y^{N_{\text{iter}}}, \boldsymbol{w}^\star)$, and $\log_{10} F(y^\star, \boldsymbol{w}^{N_{\text{iter}}})$, respectively, for $y^\star$ the sinograms without Gaussian (but with Poisson) noise, $\boldsymbol{w}^\star$ the ground truth materials, and N_{iter} the final iteration.

TABLE 5. Numerical parameters for the random subgroups of two to six materials: total number of iterations, number of iterations between reinitializations, penalty parameters, and regularization parameters.

# mats.	# iterations	reinit. interations	(μ_1, μ_2, μ_3)	(α, β)
2	100	50	(2.5, 2.5, 1e–2)/64e–4	(0.07, 0)
3	500	50	(2.5, 2.5, 1e–2)/64e–4	(0.07, 0)
4	500	50	(2.5, 2.5, 1e–2)/64e–4	(0.07, 0)
5	500	50	(2.5, 2.5, 1e–2)/64e–4	(0.07, 0)
6	500	50	(2.5, 2.5, 1e–2)/64e–4	(0.07, 0)

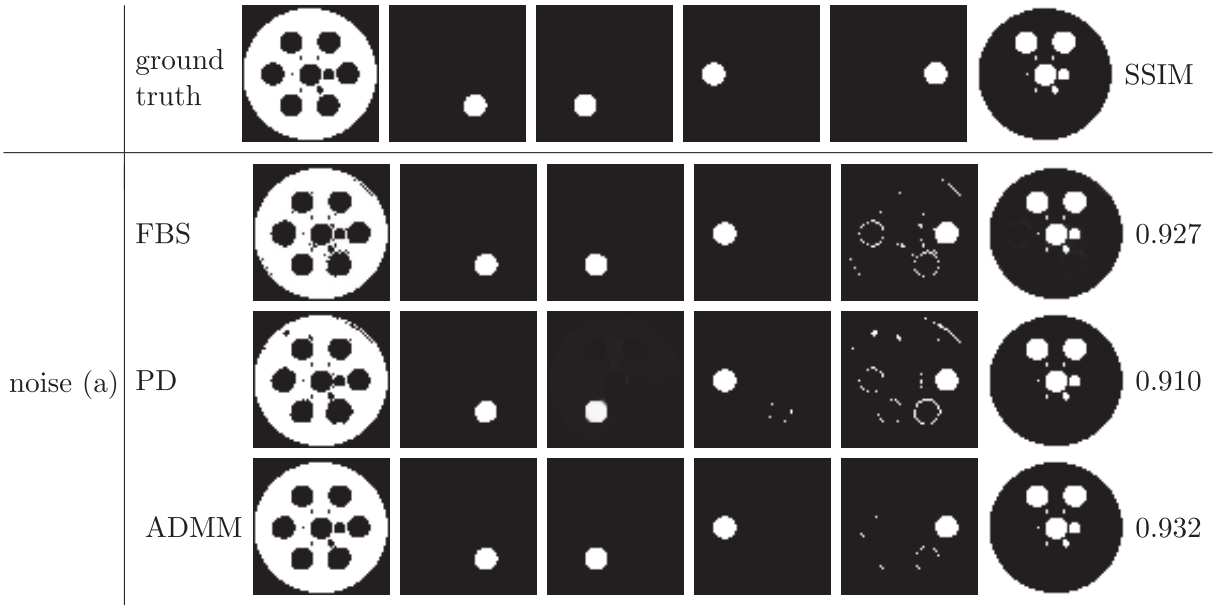

FIGURE 7. Reconstructed materials for the different algorithms with one additional material (the fifth) of almost same attenuation characteristics as the first material. Despite the strong similarity between both materials they can be almost perfectly separated.

TABLE 6. Mean CPU time in seconds and mean structural similarity index between ground truth and the reconstruction of each material for the random phantoms, broken down to the random subgroups of two to six materials.

# mats.	# phantoms	CPU (s)	mat. 1	mat. 2	mat. 3	mat. 4	mat. 5	air
2	95	34.2	0.9647	–	–	–	–	0.9649
3	179	249.2	0.8561	0.9742	–	–	–	0.9496
4	168	373.6	0.7876	0.8953	0.8652	–	–	0.9179
5	181	485.3	0.7138	0.8466	0.8992	0.8381	–	0.9345
6	77	624.8	0.6605	0.8702	0.9064	0.8641	0.7332	0.9283

5. CONCLUSION

In general for inverse problems, an improved accuracy of forward modelling should lead to improved solutions. We here covered three particular aspects that are important in several regimes of computed tomography: the polychromaticity of the X-ray source (which is particularly important if the attenuation varies strongly spatially and the X-ray dose is comparatively low), the distinction between photon counting noise and electronic noise (which is important for radiation doses in which the electronic noise becomes comparable to photon counting noise), and the explicit modelling of different material compositions. Despite the non-convexity, which is unavoidable in a model with the above ingredients, the well-posedness of the model and the convergence of the proposed algorithm could be proven. In addition, numerical examples on phantom data give satisfying results and validate the proposed model and algorithm.

Funding

This work was supported by the European Union's Horizon 2020 research and innovation programme under grant agreement No. 777826, NoMADS, as well as the Deutsche Forschungsgemeinschaft (DFG, German Research Foundation) under Germany's Excellence Strategy – EXC 2044 – Mathematics Münster: Dynamics – Geometry – Structure, and under the Collaborative Research Centre 1450–431460824, InSight, University of Münster.

References

[1] M. Abella, C. Martinez, M. Desco, J.J. Vaquero and J.A. Fessler, Simplified statistical image reconstruction for x-ray CT with beam-hardening artifact compensation. *IEEE Trans. Med. Imaging* **39** (2020) 111–118.

[2] J.D. Boerckel, D.E. Mason, A.M. McDermott and E. Alsberg, Microcomputed tomography: approaches and applications in bioengineering. *Stem Cell Res. Ther.* **5** (2014) 1–12.

[3] J.M. Borwein and S.B. Lindstrom, Meetings with Lambert W and other special functions in optimization and analysis. *Pure Appl. Funct. Anal.* **1** (2016) 361–396.

[4] L. Brabant, E. Pauwels, M. Dierick, D. Van Loo, M. Boone and L. Van Hoorebeke, A novel beam hardening correction method requiring no prior knowledge, incorporated in an iterative reconstruction algorithm. *NDT & E Int.* **51** (2012) 68–73.

[5] C. Brune, *4D imaging in tomography and optical nanoscopy*. Ph.D. thesis, Westfalishe Wilhelms-universitat Munster (2010).

[6] L. Calatroni, J.C. De Los Reyes and C.-B. Schönlieb, Infimal convolution of data discrepancies for mixed noise removal. *SIAM J. Imaging Sci.* **10** (2017) 1196–1233.

[7] A. Chambolle and T. Pock, A first-order primal-dual algorithm for convex problems with applications to imaging. *J. Math. Imaging Vis.* **40** (2011) 120–145.

[8] L. Condat, Fast projection onto the simplex and the l_1 ball. *Math. Program.* **158** (2016) 575–585.

[9] T.S. Curry, J.E. Dowdey and R.C. Murry, Jr, Christensen's Physics of Diagnostic Radiology, 4th edition. Lea and Febiger, Philadelphia (1990).

[10] B. De Man, J. Nuyts, P. Dupont, G. Marchal and P. Suetens, An iterative maximum-likelihood polychromatic algorithm for CT. *IEEE Trans. Med. Imaging* **20** (2001) 999–1008.

[11] S. Deng, Y. Zhu, H. Zhang, Q. Wang, P. Zhu, K. Zhang and P. Zhang, A method for material decomposition and quantification with grating based phase CT. *PLoS One* **16** (2021) e0245449.

[12] Q. Ding, Y. Long, X. Zhang and J.A. Fessler, Statistical image reconstruction using mixed Poisson–Gaussian noise model for X-ray CT. Preprint arXiv:1801.09533 (2018).

[13] A. Eguizabal, O. Öktem and M.U. Persson, Deep learning for material decomposition in photon-counting CT. Preprint arXiv.2208.03360 (2022).

[14] I.A. Elbakri and J.A. Fessler, Statistical image reconstruction for polyenergetic x-ray computed tomography. *IEEE Trans. Med. Imaging* **21** (2002) 89–99.

[15] I.A. Elbakri and J.A. Fessler, Segmentation-free statistical image reconstruction for polyenergetic x-ray computed tomography with experimental validation. *Phys. Med. Biol.* **48** (2003) 2453.

[16] H. Gao, H. Yu, S. Osher and G. Wang, Multi-energy CT based on a prior rank, intensity and sparsity model (PRISM). *Inverse Probl.* **27** (2011) 115012.

[17] T. Goldstein and S. Osher, The split bregman method for l1-regularized problems. *SIAM J. Imaging Sci.* **2** (2009) 323–343.

[18] C. Hamaker, K.T. Smith, D.C. Solmon and S.L. Wagner, The divergent beam X-ray transform. *Rocky Mt. J. Math.* **10** (1980) 253–283.

[19] T. Hohweiller, N. Ducros, F.C. Peyrin and B. Sixou, An ADMM algorithm for constrained material decomposition in spectral CT, in 26th European Signal Processing Conference (EUSIPCO) (2018) 71–75.

[20] Y. Hu, J.G. Nagy, J. Zhang and M.S. Andersen, Nonlinear optimization for mixed attenuation polyenergetic image reconstruction. *Inverse Probl.* **35** (2019) 064004.

[21] P. Jin, C.A. Bouman and K.D. Sauer, A model-based image reconstruction algorithm with simultaneous beam hardening correction for x-ray CT. *IEEE Trans. Comput. Imaging* **1** (2015) 200–216.

[22] K. Kalare, M. Bajpai, S. Sarkar and P. Munshi, Deep neural network for beam hardening artifacts removal in image reconstruction. *Appl. Intell.* **52** (2022) 6037–6056.

[23] B.J. Kis, Z. Sarnyai, R. Kákonyi, M. Erdélyi and G. Szabó, Single-energy material decomposition using x-ray path length estimation. *J. Comput. Assist. Tomogr.* **36** (2012) 768–777.

[24] G. Landi, E.L. Piccolomini and J.G. Nagy, A limited memory BFGS method for a nonlinear inverse problem in digital breast tomosynthesis. *Inverse Probl.* **33** (2017) 095005.

[25] K. Lange, M. Bahn and R. Little, A theoretical study of some maximum likelihood algorithms for emission and transmission tomography. *IEEE Trans. Med. Imaging* **6** (1987) 106–114.

[26] A. Lanza, S. Morigi, F. Sgallari and Y.-W. Wen, Image restoration with Poisson–Gaussian mixed noise. *Comput. Methods Biomech. Biomed. Eng. Imaging Vis.* **2** (2014) 12–24.

[27] Y. Liao, Y. Wang, S. Li, J. He, D. Zeng, Z. Bian and J. Ma, Pseudo dual energy CT imaging using deep learning-based framework: basic material estimation, in Medical Imaging 2018: Physics of Medical Imaging, edited by J.Y. Lo, T.G. Schmidt and G.-H. Chen. Vol. 10573 of *International Society for Optics and Photonics*. SPIE (2018) 105734N.

[28] J. Liu and H. Gao, Material reconstruction for spectral computed tomography with detector response function. *Inverse Probl.* **32** (2016) 114001.

[29] S. Luo, H. Wu, Y. Sun, J. Li, G. Li and N. Gu, A fast beam hardening correction method incorporated in a filtered back-projection based map algorithm. *Phys. Med. Biol.* **62** (2017) 1810.

[30] A. Markoe, Analytic Tomography. Vol. 13. Cambridge University Press, Cambridge (2006).

[31] C.H. McCollough, S. Leng, L. Yu and J.G. Fletcher, Dual- and multi-energy CT: principles, technical approaches, and clinical applications. *Radiology* **276** (2015) 637–653.

[32] N. Menvielle, Y. Goussard, D. Orban and G. Soulez, Reduction of beam-hardening artifacts in x-ray CT, in 2005 IEEE Engineering in Medicine and Biology 27th Annual Conference. IEEE (2005).

[33] D. Modgil, D.S. Rigie, Y. Wang, X. Xiao, P.A. Vargas and P.J. La Rivière, Material identification in x-ray microscopy and micro CT using multi-layer, multi-color scintillation detectors. *Phys. Med. Biol.* **60** (2015) 8025.

[34] A.M. Müller, L. Butzhammer and T. Hausotte, Implementation of a beam hardening correction method for mono material parts using a linearization technique, in International Symposium on Digital Industrial Radiology and Computed Tomography, Fürth, Germany (2019).

[35] J. Nuyts, B. De Man, J.A. Fessler, W. Zbijewski and F.J. Beekman, Modelling the physics in the iterative reconstruction for transmission computed tomography. *Phys. Med. Biol.* **58** (2013) R63.

[36] C. Olasz, L.G. Varga and A. Nagy, Beam hardening artifact removal by the fusion of FBP and deep neural networks, in Thirteenth International Conference on Digital Image Processing (ICDIP 2021), edited by X. Jiang and H. Fujita. Vol. 11878 of *International Society for Optics and Photonics*. SPIE (2021) 1187817.

[37] G. Papanikos, *Variational image reconstruction methods for tomography – PET and transmission CT with mixed Poisson–Gaussian noise*. Ph.D. thesis, University of Nottingham (2020).

[38] A. Perelli and S.A. Martin, Regularization by denoising sub-sampled Newton method for spectral CT multi-material decomposition. *Philos. Trans. A Math. Phys. Eng. Sci.* **379** (2021) 20200191.

[39] G. Perez, S. Ament, C. Gomes and M. Barlaud, Efficient projection algorithms onto the weighted ℓ_1 ball. *Artif. Intell.* **306** (2022) 14.

[40] T. Pock and A. Chambolle, Diagonal preconditioning for first order primal-dual algorithms in convex optimization, in 2011 International Conference on Computer Vision (2011) 1762–1769.

[41] L.I. Rudin, S. Osher and E. Fatemi, Nonlinear total variation based noise removal algorithms. *Phys. D* **60** (1992) 259–268.

[42] C. Ruth and P.M. Joseph, Estimation of a photon energy spectrum for a computed tomography scanner. *Med. Phys.* **24** (1997) 695–702.

[43] Y. Saad and M.H. Schultz, GMRES: a generalized minimal residual algorithm for solving nonsymmetric linear systems. *SIAM J. Sci. Stat. Comput.* **7** (1986) 856–869.

[44] A. Sawatzky, *(Nonlocal) total variation in medical imaging*. Ph.D. thesis, Westfalische Wilhelms-Universitat Munster (2011).

[45] C.O. Schirra, B. Brendel, M.A. Anastasio and E. Roessl, Spectral CT: a technology primer for contrast agent development. *Contrast Media Mol. Imaging* **9** (2014) 62–70.

[46] R. Solem, T. Dreier, I. Goncalves and M. Bech, Material decomposition in low-energy micro-CT using a dual-threshold photon counting x-ray detector. *Front. Phys.* **9** (2021) 673843.

[47] X.-C. Tai and C. Wu, Augmented Lagrangian method, dual methods and split Bregman iteration for ROF model, in Scale Space and Variational Methods in Computer Vision, edited by X.-C. Tai, K. Mørken, M. Lysaker and K.-A. Lie. Springer, Berlin (2009) 502–513.

[48] L.N. Trefethen and D. Bau, III, Numerical Linear Algebra. Society for Industrial and Applied Mathematics (SIAM), Philadelphia (2022). With a foreword by James G. Nagy.
[49] J. Wang, X. Duan and C.H. McCollough, Material Decomposition and Post-Processing: History and Basic Principles. Springer International Publishing, Cham (2022) 3–14.
[50] M. Wu, Q. Yang, A. Maier and R. Fahrig, A practical statistical polychromatic image reconstruction for computed tomography using spectrum binning, in Medical Imaging 2014: Physics of Medical Imaging, edited by B.R. Whiting and C. Hoeschen. SPIE (2014).
[51] S. Xu, A. Uneri, A.J. Khanna, J.H. Siewerdsen and J.W. Stayman, Polyenergetic known-component CT reconstruction with unknown material compositions and unknown x-ray spectra. *Phys. Med. Biol.* **62** (2017) 3352.
[52] Y. Xue, C. Luo, Y. Jiang, P. Yang, X. Hu, Q. Zhou, J. Wang, X. Hu, K. Sheng and T. Niu, Image domain multi-material decomposition using single energy CT. *Phys. Med. Biol.* **65** (2020) 065014.
[53] Y. Xue, W. Qin, C. Luo, P. Yang, Y. Jiang, T. Tsui, H. He, L. Wang, J. Qin, Y. Xie and T. Niu, Multi-material decomposition for single energy CT using material sparsity constraint. *IEEE Trans. Med. Imaging* **40** (2021) 1303–1318.
[54] C.H. Yan, R.T. Whalen, G.S. Beaupré, S.Y. Yen and S. Napel, Reconstruction algorithm for polychromatic CT imaging: application to beam hardening correction. *IEEE Trans. Med. Imaging* **19** (2000) 1–11.
[55] Q. Yang, M. Wu, A. Maier, J. Hornegger and R. Fahrig, Evaluation of Spectrum Mismatching Using Spectrum Binning for Statistical Polychromatic Reconstruction in CT. Springer, Berlin (2014) 42–47.
[56] Y. Yao, L. Li and Z. Chen, Dynamic-dual-energy spectral CT for improving multi-material decomposition in image-domain. *Phys. Med. Biol.* **64** (2019) 135006.
[57] J. Zhang, Y. Hu and J.G. Nagy, A scaled gradient method for digital tomographic image reconstruction. *Inverse Probl. Imaging* **12** (2018) 239–259.
[58] W. Zhao, D. Li, K. Niu, W. Qin, H. Peng and T. Niu, Robust beam hardening artifacts reduction for computed tomography using spectrum modeling. *IEEE Trans. Comput. Imaging* **5** (2019) 333–342.
[59] W. Zhao, T. Lv, P. Gao, L. Shen, X. Dai, K. Cheng, M. Jia, Y. Chen and L. Xing, A deep learning approach for dual-energy CT imaging using a single-energy CT data, in 15th International Meeting on Fully Three-Dimensional Image Reconstruction in Radiology and Nuclear Medicine, edited S. Matej and S.D. Metzler. Vol. 11072 of *International Society for Optics and Photonics*. SPIE (2019) 1107222.

Appendix A. An alternating minimization with primal-dual updates

While the previous algorithm is quite fast and efficient for noisy data and high regularization, for low noise we need to change it. We still employ the same update for y, but the update of $\boldsymbol{w}$ will be performed by the primal-dual iteration of Chambolle and Pock [7]. The overall algorithm is given in Algorithm 2.

A.1. Primal-dual update of $\boldsymbol{w}$

To this end we write the $\boldsymbol{w}$-dependent part of the energy F as

$$\frac{F(y,\boldsymbol{w}) - \frac{1}{2\sigma^2}\int_\Sigma \Big(f - \int_{E_{\min}}^{E_{\max}} y \,\mathrm{d}\mathcal{L}^1\Big)^2 \mathrm{d}\mathcal{H}^n}{\alpha} = F_1((\mathcal{D},\nabla)\boldsymbol{w}) + F_2(\boldsymbol{w}) \quad \text{with}$$

Algorithm 2. Chambolle–Pock-based algorithm for polyenergetic CT reconstruction.

initialize $y^0, \boldsymbol{w}^0, \boldsymbol{\phi}, \boldsymbol{\psi}$
for $k = 1, \dots$ **do**
  calculate y^k *via* (3.1)
  initialize Chambolle–Pock iteration with $\overline{\boldsymbol{w}} = \boldsymbol{w}^{k-1}$, $\boldsymbol{w} = \boldsymbol{w}^{k-1}$
  for $i = 1, \dots, \mathrm{iter}_{\mathrm{CP}}$ **do**
    perform a Chambolle–Pock update (A.1) in primal $(\boldsymbol{w}, \overline{\boldsymbol{w}})$ & dual variables $(\boldsymbol{\phi}, \boldsymbol{\psi})$
  end for
  set $\boldsymbol{w}^k = \boldsymbol{w}$
  if reinitialization condition **then**
    run a reinitialization heuristic (see Sect. 3.4) to avoid spurious local minima
  end if
end for

$$
\begin{aligned}
F_1(\boldsymbol{u}, \boldsymbol{X}) &= F_{11}(\boldsymbol{u}) + F_{12}(\boldsymbol{X}) \\
&= \frac{1}{\alpha} \int_\Sigma \int_{E_{\min}}^{E_{\max}} d_{\mathrm{KL}}\left(y, I_0 \exp\left(-\sum_{i=1}^{N_{\mathrm{mat}}} g_i u_i\right)\right) \mathrm{d}\mathcal{L}^1 \, \mathrm{d}\mathcal{H}^n + \sum_{i=1}^{N_{\mathrm{mat}}} \|X_i\|_{\mathcal{M}}, \\
F_2(\boldsymbol{w}) &= F_{21}(\boldsymbol{w}) + F_{22}(\boldsymbol{w}) \\
&= \frac{\beta}{\alpha} R_2(\boldsymbol{w}) + \int_\Omega \iota_\Delta(\boldsymbol{w}) \, \mathrm{d}\mathcal{L}^n,
\end{aligned}
$$

where $\|X\|_{\mathcal{M}}$ denotes the total variation or norm of the vector-valued measure X. The corresponding primal-dual iteration with dual variables $\boldsymbol{\phi} = (\phi_1, \dots, \phi_{N_{\mathrm{mat}}}) : \Sigma \to \mathbb{R}^{N_{\mathrm{mat}}}$ and $\psi = (\psi_1, \dots, \psi_{N_{\mathrm{mat}}}) : \Sigma \to (\mathbb{R}^2)^{N_{\mathrm{mat}}}$, step sizes $\tau > 0$ and $\rho_1, \rho_2 > 0$ for primal descent and dual ascent as well as relaxation parameter $\theta \in [0, 1]$ reads

$$
\left.
\begin{aligned}
\boldsymbol{\phi}^{\mathrm{new}} &= \mathbf{prox}_{\rho_1 F_{11}^*}\left(\boldsymbol{\phi}^{\mathrm{old}} + \rho_1 \mathcal{D} \overline{\boldsymbol{w}}^{\mathrm{old}}\right), \\
\boldsymbol{\psi}^{\mathrm{new}} &= \mathbf{prox}_{\rho_2 F_{12}^*}\left(\boldsymbol{\psi}^{\mathrm{old}} + \rho_2 \nabla \overline{\boldsymbol{w}}^{\mathrm{old}}\right), \\
\boldsymbol{w}^{\mathrm{new}} &= \mathbf{prox}_{\tau F_{22}}\left(\boldsymbol{w}^{\mathrm{old}} - \tau(\mathcal{D}^* \boldsymbol{\phi}^{\mathrm{new}} + \nabla^* \boldsymbol{\psi}^{\mathrm{new}}) - \tau F_{21}'(\boldsymbol{w}^{\mathrm{old}})\right), \\
\overline{\boldsymbol{w}}^{\mathrm{new}} &= \boldsymbol{w}^{\mathrm{new}} + \theta(\boldsymbol{w}^{\mathrm{new}} - \boldsymbol{w}^{\mathrm{old}}).
\end{aligned}
\right\} \tag{A.1}
$$

Note that $\nabla^* = -\operatorname{div}$. To ensure stability, the step sizes have to be chosen small enough with respect to the norms of the linear operators. A feasible choice from [40] is $\rho_2 = \frac{1}{2}$ (the reciprocal of the absolute row sum of the discretized derivative operator ∇), $\rho_1 = \frac{1}{\operatorname{diam}\Omega}$ (the reciprocal of the maximum absolute row sum of the discretized beam transform $\mathcal{D}$), and $\tau = \frac{1}{4+2\pi}$ (the reciprocal of the maximum absolute row sum of the discretization of $(\mathcal{D}^*, \nabla^*)$: in 2D the absolute row sum of the discrete ∇^* is 4, and our curve $\boldsymbol{\xi}$ is a half-circle of radius 2 around the unit disc Ω so that $|\boldsymbol{z} - \boldsymbol{x}| \geq 1$ for all $(\boldsymbol{z}, \boldsymbol{x}) \in \boldsymbol{\xi} \times \Omega$ and thus the integral in (2.2) for $\boldsymbol{w} \equiv 1$ can be bounded by 2π – in general one could of course also compute these values numerically). The proximal operator $\mathbf{prox}_{\tau F_{22}}$ merely is the pointwise Euclidean projection onto the probability simplex Δ, for which efficient and simple algorithms exist [8]. As for $\mathbf{prox}_{\rho_2 F_{12}^*}$ it is straightforward to compute the Legendre–Fenchel conjugate $F_{12}^*(\boldsymbol{\psi}) = 0$ if $|\psi_i| \leq 1$ almost everywhere on Σ for all i and $F_{12}^*(\boldsymbol{\psi}) = \infty$ else. Thus the corresponding proxial operator reads

$$
\mathbf{prox}_{\rho_2 F_{12}^*}(\boldsymbol{\psi})(\boldsymbol{x}) = \left(\frac{\psi_i(\boldsymbol{x})}{|\psi_i(\boldsymbol{x})|} \min\{1, |\psi_i(\boldsymbol{x})|\}\right)_{i=1,\dots,N_{\mathrm{mat}}}.
$$

As for the proximal operator of F_{11}^* we exploit the equivalence

$$
\boldsymbol{\xi} = \mathbf{prox}_{\rho_1 F_{11}^*}(\boldsymbol{\phi}) \quad \Leftrightarrow \quad \boldsymbol{\xi} \in \partial F_{11}\left(\frac{\boldsymbol{\phi} - \boldsymbol{\xi}}{\rho_1}\right) = \frac{1}{\alpha} \int_{E_{\min}}^{E_{\max}} y\boldsymbol{g} - I_0 \boldsymbol{g} \exp\left(\sum_{i=1}^{N_{\mathrm{mat}}} \frac{\xi_i - \phi_i}{\rho_1} g_i\right) \mathrm{d}\mathcal{L}^1,
$$

where for ease of notation we identified the subdifferential with its single element. This equation can be solved for $\boldsymbol{\xi}$ separately and independently at all $(\boldsymbol{x}, \boldsymbol{\theta}) \in \Sigma$. Indeed, abbreviating for fixed $(\boldsymbol{x}, \boldsymbol{\theta}) \in \Sigma$

$$\begin{aligned} B &= \frac{\boldsymbol{g}}{\rho_1} : (E_{\min}, E_{\max}) \to \mathbb{R}^{N_{\mathrm{mat}}}, \\ s(\boldsymbol{x}, \boldsymbol{\theta}) &= \frac{\rho_1}{\alpha} I_0 \exp\left(-\frac{1}{\rho_1} \sum_{i=1}^{N_{\mathrm{mat}}} \phi_i(\boldsymbol{x}, \boldsymbol{\theta}) g_i \right) : (E_{\min}, E_{\max}) \to \mathbb{R}, \\ y &= \frac{\rho_1}{\alpha} y(\boldsymbol{x}, \boldsymbol{\theta}) : \Sigma \to \mathbb{R}, \end{aligned}$$

it can readily be checked that the sought $\xi(\boldsymbol{x}, \boldsymbol{\theta}) \in \mathbb{R}^{N_{\mathrm{mat}}}$ is the unique minimizer of the convex functional

$$\frac{1}{2} \left| \xi(\boldsymbol{x}, \boldsymbol{\theta}) - \int_{E_{\min}}^{E_{\max}} yB \, \mathrm{d}\mathcal{L}^1 \right|^2 + \int_{E_{\min}}^{E_{\max}} s(\boldsymbol{x}, \boldsymbol{\theta}) \exp(B \cdot \xi(\boldsymbol{x}, \boldsymbol{\theta})) \, \mathrm{d}\mathcal{L}^1.$$

Discretizing the integral with numerical quadrature, this turns into an expression of the form

$$\frac{1}{2} \left| \xi(\boldsymbol{x}, \boldsymbol{\theta}) - B^T y \right|^2 + s^T \exp(B\xi(\boldsymbol{x}, \boldsymbol{\theta})), \tag{A.2}$$

where the exponential is applied componentwise and for simplicity we used the same symbols for the matrices s, B and the vector y resulting from discretizing the corresponding continuous objects. Thus we obtain

$$\xi(\boldsymbol{x}, \boldsymbol{\theta}) = \mathbf{prox}_h(B^T y) \quad \text{for} \quad h(\boldsymbol{\xi}) = s^T \exp(B\xi).$$

The computation of this proximal operator is detailed in the next paragraph.

A.2. Proximal operator for vectors of exponentials

The minimizer $\boldsymbol{\xi} \in \mathbb{R}^{N_{\mathrm{mat}}}$ of (A.2) is computed *via* the corresponding Newton iteration

$$\boldsymbol{\xi}^{n+1} = \boldsymbol{\xi}^n - (I + B^T \mathrm{diag}(\exp(B\boldsymbol{\xi}^n + \log s))B)^{-1}(\boldsymbol{\xi}^n + B^T \exp(B\boldsymbol{\xi}^n + \log s) - B^T y),$$

where exponential and logarithm are applied componentwise and $\mathrm{diag}(v)$ for a vector v indicates the diagonal matrix with diagonal v. Note that for numerical stability it turns out to be important to add $\log s$ inside the exponential rather than multiplying with s. As initialization we pick

$$\boldsymbol{\xi}^1 = B^\dagger(\log y - \max\{\log s, -\delta\})$$

in which $B^\dagger$ denotes the Moore–Penrose inverse of B and δ is a fixed parameter introduced to safeguard the case of vanishing s. In our simulations we take $\delta = 1000$. Alternatively one can also initialize with the optimal $\boldsymbol{\xi}$ from the previous primal-dual iteration. The reasoning for this initialization is that the solution $\boldsymbol{\xi}$ must be very small in absolute value due to the exponential amplification; thus the optimality condition is approximately $B^T \exp(B\boldsymbol{\xi} + \log s) - B^T y = 0$ of which $\boldsymbol{\xi}^1$ is an approximate solution.

Appendix B. ADMM approach

Yet another alternative (which only requires inner iterations for solving a linear system and a pointwise nonlinear equation) is the following implementation *via* the alternating direction method of multipliers (ADMM).

To this end we rewrite the minimization of F as

$$\min\{\mathcal{R}(\boldsymbol{X}, \tilde{\boldsymbol{w}}) + \mathcal{H}(y, \boldsymbol{z}) \,|\, y : [E_{\min}, E_{\max}] \times \Sigma \to \mathbb{R}, \boldsymbol{w} : \Omega \to \mathbb{R}^{N_{\mathrm{mat}}},$$

$$\boldsymbol{X} = \nabla \boldsymbol{w}, \ \tilde{\boldsymbol{w}} = \boldsymbol{w}, \ \boldsymbol{z} = \mathcal{D}\boldsymbol{w}\}, \text{ where}$$

$$\mathcal{R}(\boldsymbol{X}, \tilde{\boldsymbol{w}}) = \alpha \sum_{i=1}^{N_{\mathrm{mat}}} \|X_i\|_{\mathcal{M}} + \int_\Omega \iota_\Delta(\tilde{\boldsymbol{w}}) \mathrm{d}\mathcal{L}^n + \beta R_2(\tilde{\boldsymbol{w}}),$$

$$\mathcal{H}(y,\boldsymbol{z}) = \frac{1}{2\sigma^2}\int_\Sigma \left(f - \int_{E_{\min}}^{E_{\max}} y \mathrm{d}\mathcal{L}^1\right)^2 \mathrm{d}\mathcal{H}^n + \int_\Sigma \int_{E\min}^{E_{\max}} d_{KL}\Big(y, \hat{\mathfrak{I}}(\boldsymbol{z})\Big)\mathrm{d}\mathcal{L}^1\mathrm{d}\mathcal{H}^n$$

for $\hat{\mathfrak{I}}(\boldsymbol{z}) = I_0 \exp(-\sum_{i=1}^{N_{\mathrm{mat}}} g_i z_i)$. We form the augmented Lagrangian

$$\begin{aligned}\mathcal{L}(y,\boldsymbol{w},\tilde{\boldsymbol{w}},\boldsymbol{X},\boldsymbol{z};\ \boldsymbol{\Lambda},\boldsymbol{\lambda}_1,\boldsymbol{\lambda}_2) = \mathcal{R}(\boldsymbol{X},\tilde{\boldsymbol{w}}) + \mathcal{H}(y,\boldsymbol{z}) + \langle \boldsymbol{\Lambda}, \boldsymbol{X} - \nabla \boldsymbol{w}\rangle + \frac{\mu_1}{2}\|\boldsymbol{X} - \nabla \boldsymbol{w}\|_{L^2}^2 \\ + \langle \boldsymbol{\lambda}_1, \tilde{\boldsymbol{w}} - \boldsymbol{w}\rangle + \frac{\mu_2}{2}\|\tilde{\boldsymbol{w}} - \boldsymbol{w}\|_{L^2}^2 + \langle \boldsymbol{\lambda}_2, \boldsymbol{z} - \mathcal{D}\boldsymbol{w}\rangle + \frac{\mu_3}{2}\|\boldsymbol{z} - \mathcal{D}\boldsymbol{w}\|_{L^2}^2\end{aligned}$$

with Lagrange multipliers $\boldsymbol{\Lambda} : \Omega \to \mathbb{R}^{N_{\mathrm{mat}}\times n}$, $\boldsymbol{\lambda}_1 : \Omega \to \mathbb{R}^{N_{\mathrm{mat}}}$ and $\boldsymbol{\lambda}_2 : \Sigma \to \mathbb{R}^{N_{\mathrm{mat}}}$ and penalty weights $\mu_1, \mu_2, \mu_3 > 0$. The minimization problem is solved by alternatingly minimizing the augmented Lagrangian with respect to the primal variables $\boldsymbol{w}$, $\tilde{\boldsymbol{w}}$, $\boldsymbol{X}$, y, and $\boldsymbol{z}$, and then updating the Lagrange multipliers $\boldsymbol{\Lambda}$, $\boldsymbol{\lambda}_1$ and $\boldsymbol{\lambda}_2$, known as ADMM,

$$\boldsymbol{w}^k = \operatorname*{argmin}_{\boldsymbol{w}} \mathcal{L}(y^{k-1}, \boldsymbol{w}, \tilde{\boldsymbol{w}}^{k-1}, \boldsymbol{X}^{k-1}, \boldsymbol{z}^{k-1}; \boldsymbol{\Lambda}^{k-1}, \boldsymbol{\lambda}_1^{k-1}, \boldsymbol{\lambda}_2^{k-1}), \tag{B.1}$$

$$(\tilde{\boldsymbol{w}}^k, \boldsymbol{X}^k, y^k, \boldsymbol{z}^k) = \operatorname*{argmin}_{(\tilde{\boldsymbol{w}},\boldsymbol{X},y,\boldsymbol{z})} \mathcal{L}(y, \boldsymbol{w}^k, \tilde{\boldsymbol{w}}, \boldsymbol{X}, \boldsymbol{z}; \boldsymbol{\Lambda}^{k-1}, \boldsymbol{\lambda}_1^{k-1}, \boldsymbol{\lambda}_2^{k-1}), \tag{B.2}$$

$$(\boldsymbol{\Lambda}^k, \boldsymbol{\lambda}_1^k, \boldsymbol{\lambda}_2^k) = (\boldsymbol{\Lambda}^{k-1} + \mu_1(\boldsymbol{X}^k - \nabla \boldsymbol{w}^k), \boldsymbol{\lambda}_1^{k-1} + \mu_2(\tilde{\boldsymbol{w}}^k - \boldsymbol{w}^k), \boldsymbol{\lambda}_2^{k-1} + \mu_3(\boldsymbol{z}^k - \mathcal{D}\boldsymbol{w}^k)). \tag{B.3}$$

The solution $\boldsymbol{w}^k$ can readily be shown to satisfy the linear optimality condition

$$(\mu_2 I + \mu_3 \mathcal{D}^*\mathcal{D} - \mu_1 \Delta) w_i^k = \lambda_{1,i}^{k-1} + \mu_2 \tilde{w}_i^{k-1} + \mathcal{D}^*\Big(\lambda_{2,i}^{k-1} + \mu_3 z_i^{k-1}\Big) - \operatorname{div}(\Lambda_i^{k-1} + \mu_1 X_i^{k-1}) \tag{B.4}$$

for $i = 1, \ldots, N_{\mathrm{mat}}$ (where we assume periodic boundary conditions for simplicity and I represents the identity operator).

This linear system of equations is solved using the preconditioned generalized minimal residual method (preconditioned GMRES, see [43] or the textbook [48]) with preconditioner

$$P = \mathcal{F}^{-1}\Big(\mu_2 \mathcal{F}(I) + \mu_3 c \mathcal{F}\Big((-\Delta)^{-\frac{1}{2}}\Big) - \mu_1 \mathcal{F}(\Delta)\Big).$$

Above, $\mathcal{F}(A)$ denotes the representation of a linear operator A in Fourier space. Since $-\Delta$ is diagonal in Fourier space, P is straightforward and highly efficient to invert. The choice of the term $(-\Delta)^{-1/2}$ is motivated by $\mathcal{D}^*\mathcal{D}$ equalling that linear operator on an unbounded domain. The components X_i^k of $\boldsymbol{X}^k$ are readily computed for $i = 1, \ldots, N_{\mathrm{mat}}$ *via*

$$X_i^k(x) = \mathbf{prox}_{\frac{\alpha|\cdot|}{\mu_1}}\left(\nabla w_i^k(x) - \frac{\Lambda_i^{k-1}(x)}{\mu_1}\right) \text{ with } \mathbf{prox}_{\frac{\alpha|\cdot|}{\mu_1}} \boldsymbol{v} = \max\{0, |\boldsymbol{v}| - \tfrac{\alpha}{\mu_1}\}\tfrac{\boldsymbol{v}}{|\boldsymbol{v}|}. \tag{B.5}$$

For given $\boldsymbol{z}^k$, the optimal value y^k is due to Lemma 2.6 given as $y^k(x) = y(\boldsymbol{z}^k(x))$ for

$$y(\boldsymbol{z}) = \hat{\mathfrak{I}}(\boldsymbol{z}) \exp\left(\tfrac{f}{\sigma^2} - W_0\left(\frac{\hat{\mathcal{F}}(\boldsymbol{z})}{\sigma^2}\exp(f/\sigma^2)\right)\right) = \hat{\mathfrak{I}}(\boldsymbol{z}) \frac{W_0\Big(\hat{\mathfrak{I}}(\boldsymbol{z})\frac{\exp(f/\sigma^2)}{\sigma^2}\Big)}{\hat{\mathfrak{I}}(\boldsymbol{z})/\sigma^2}, \tag{B.6}$$

where we abbreviated $\hat{\mathcal{F}}(\boldsymbol{z}) = \int_{E_{\min}}^{E_{\max}} \hat{\mathfrak{I}}(\boldsymbol{z})\,\mathrm{d}E$. Having thus eliminated y^k, it still remains to minimize for $\boldsymbol{z}^k$. Defining $H^k(y,\boldsymbol{z}) = \mathcal{L}(y, \boldsymbol{w}^k, \tilde{\boldsymbol{w}}, \boldsymbol{X}, \boldsymbol{z}; \boldsymbol{\Lambda}^{k-1}, \boldsymbol{\lambda}_1^{k-1}, \boldsymbol{\lambda}_2^{k-1})$, the optimality condition for $\boldsymbol{z}^k$ becomes

$$\begin{aligned}0 &= \tfrac{\mathrm{d}}{\mathrm{d}\boldsymbol{z}} H^k(y(\boldsymbol{z}^k), \boldsymbol{z}^k) = \partial_y H^k(y(\boldsymbol{z}^k), \boldsymbol{z}^k)\tfrac{\mathrm{d}y(\boldsymbol{z}^k)}{\mathrm{d}\boldsymbol{z}} + \partial_{\boldsymbol{z}} H^k(y(\boldsymbol{z}^k), \boldsymbol{z}^k) = \partial_{\boldsymbol{z}} H^k(y(\boldsymbol{z}^k), \boldsymbol{z}^k) \\ &= \boldsymbol{\lambda}_2 + \mu_3(\boldsymbol{z}^k - \mathcal{D}\boldsymbol{w}^k) + \int_{E_{\min}}^{E_{\max}} \Big(y(\boldsymbol{z}^k) - \hat{\mathfrak{I}}(\boldsymbol{z}^k)\Big)\boldsymbol{g}\,\mathrm{d}\mathcal{L}^1 =: h(\boldsymbol{z}),\end{aligned}$$

which is solved for $\boldsymbol{z}^k$ pointwise on Σ by a rapidly converging (damped) Newton iteration

$$\boldsymbol{z}^{k,\mathrm{new}} = \boldsymbol{z}^{k,\mathrm{old}} - \gamma^k (Dh(\boldsymbol{z}^{k,\mathrm{old}}))^{-1} h(\boldsymbol{z}^{k,\mathrm{old}}) \tag{B.7}$$

with damping factor $\gamma^k = \min\left(1, \frac{10}{\|Dh^{-1}(\boldsymbol{z}^{k,\text{old}})h(\boldsymbol{z}^{k,\text{old}})\|_2}\right)$. This factor just ensures that in the quadratic convergence regime close to the zero the Newton step (*i.e.* $\gamma^k = 1$) is taken while otherwise the size of the update never exceeds norm 10 (an arbitrary choice just preventing too large steps). For the reader's convenience we provide the Newton operator

$$\nabla h(\boldsymbol{z}) = \mu_3 - \left(\frac{W_0\left(\frac{\exp(f/\sigma^2)}{\sigma^2}\hat{\mathcal{F}}(\boldsymbol{z})\right)}{\hat{\mathcal{F}}(\boldsymbol{z})/\sigma^2} - 1\right)\int_{E_{\min}}^{E_{\max}} \boldsymbol{g}\otimes\boldsymbol{g}\,\hat{\mathcal{J}}(\boldsymbol{z})\,\mathrm{d}\mathcal{L}^1 + \frac{W_0^2\left(\frac{\exp(f/\sigma^2)}{\sigma^2}\hat{\mathcal{F}}(\boldsymbol{z})\right)}{\hat{\mathcal{F}}(\boldsymbol{z})^2\left(1+W_0\left(\frac{\exp(f/\sigma^2)}{\sigma^2}\hat{\mathcal{F}}(\boldsymbol{z})\right)\right)/\sigma^2}\int_{E_{\min}}^{E_{\max}} \boldsymbol{g}\,\hat{\mathcal{J}}(\boldsymbol{z})\,\mathrm{d}\mathcal{L}^1\otimes\int_{E_{\min}}^{E_{\max}} \boldsymbol{g}\,\hat{\mathcal{J}}(\boldsymbol{z})\,\mathrm{d}\mathcal{L}^1.$$

Finally, the optimization problem in $\tilde{\boldsymbol{w}}$ is nonconvex, so instead of a full optimization we actually replace the nonconvex term $R_2(\tilde{\boldsymbol{w}})$ with its first order Taylor expansion at $\tilde{\boldsymbol{w}}^{k-1}$ (which corresponds to just doing an explicit gradient step in the nonconvex term) and thereby obtain

$$\tilde{\boldsymbol{w}}^k(\boldsymbol{x}) = \operatorname*{argmin}_{\tilde{\boldsymbol{w}}(\boldsymbol{x})} \frac{\mu_2}{2}\left|\tilde{\boldsymbol{w}}(\boldsymbol{x}) - \frac{\mu_2\boldsymbol{w}^k(\boldsymbol{x}) - \boldsymbol{\lambda}_1^{k-1}(\boldsymbol{x}) + \beta(\tilde{\boldsymbol{w}}^{k-1}(\boldsymbol{x}) - \frac{\mathbf{1}_{N_{\text{mat}}}}{N_{\text{mat}}})}{\mu_2}\right|^2 + \iota_\Delta(\tilde{\boldsymbol{w}}(\boldsymbol{x})), \tag{B.8}$$

a projection onto the probability simplex, for which efficient non-iterative algorithms exist [8]. The full scheme is summarized in Algorithm 3.

Algorithm 3. ADMM for poly-energetic reconstruction.

repeat
- calculate w_i^k *via* solving the linear system (B.4) with preconditioned GMRES
- calculate X_i^k *via* (B.5)
- calculate $\boldsymbol{z}^k$ *via* the damped Newton method (B.7)
- calculate $y^k = y(\boldsymbol{z}^k)$ by (B.6)
- calculate $\tilde{\boldsymbol{w}}^k$ *via* solving (B.8)
- calculate the dual variables $\boldsymbol{\Lambda}^k$, $\boldsymbol{\lambda}_1^k$ and $\boldsymbol{\lambda}_2^k$ *via* (B.3)
- **if** reinitialization condition **then**
  - run a reinitialization heuristic (see Sect. 3.4) to avoid spurious local minima
- **end if**
- $k \leftarrow k+1$

until $\|\tilde{\boldsymbol{w}}^k - \tilde{\boldsymbol{w}}^{k-1}\|_{L^2}/\|\tilde{\boldsymbol{w}}^{k-1}\|_{L^2} <$ tolerance